DEFORMATION OF TWO PHASE AL-FE AND AL-NI ALLOYS

DEFORMATION OF TWO PHASE AL-FE AND AL-NI ALLOYS

By

BRIAN EDWARD SNEEK, B. Eng

A Thesis

Submitted to the School of Graduate Studies

in Partial Fulfillment of the Requirements

for the Degree

Master of Engineering

McMaster University

MASTER OF ENGINEERING (1996) McMaster University

(Materials Science and Engineering) Hamilton, Ontario

TITLE: Deformation of Two Phase Al-Fe and Al-Ni Alloys

AUTHOR: Brian Edward Sneek, B. Eng (McMaster University)

SUPERVISOR: Professor G.C. Weatherly

NUMBER OF PAGES: xii, 76

Abstract

Aluminum alloys are presently used extensively as a conductor material for overhead transmission wires. Their lack of strength must be compensated by using a reinforcing agent, namely steel. The aim of this thesis was to investigate the possibility of deforming Al-Fe and Al-Ni alloys in order to produce high strength, high conductivity wire product. The main goal was to produce a two phase Al alloy wire with adequate strength so that the wire would be self supporting as an overhead electrical power transmission line.

The Al-Fe and Al-Ni two phase alloy rods were Ohno cast to provide directional solidification. In both alloys, wire drawing was unsuccessful due to fiber fracture and damage accumulation during drawing. The Al-Fe alloy was subjected to hydrostatic extrusion in an attempt to induce co-deformation of the matrix material and the brittle intermetallic second phase, Al_6Fe. Hydrostatic extrusion proved to be successful in inducing some deformation of the Al_6Fe and provided valuable initial insight into the investigation of the deformation of Al_6Fe.

The final stage in the development of an aluminum alloy for use as a self supporting overhead transmission wire was the development of a "macrocomposite". This macrocomposite was a combination of an Fe rod 4 mm in diameter and a tube of aluminum 8 mm in diameter. This macrocomposite was successfully cold worked to achieve an overall yield strength of 395 MPa.

Acknowledgments

The author would like to thank his supervisor, Dr. G. C. Weatherly for the freedom to carry out his research project, helpful advice and discussion when needed. He is also sincerely grateful to Dr. J. D. Embury for his guidance and valuable assistance during this work.

Special thanks to Dr. A. McLean and Mr. H. Soda for use of their equipment at The University of Toronto. At McMaster, the help of Muriel Veron with TEM, Mrs. Teresa Castillo with SEM and Mr. J. D. Garrett with materials preparation are thankfully acknowledged.

Finally, the author wishes to thank his family, the DeMorest's and his fellow graduate students for their helpful discussions and inspiration to keep going. His stay at McMaster University has been an enjoyable one.

Dedication

To my future wife Laurie,

who, with her love, patience and support has provided me with the ideal conditions to succeed. Without her, none of this would have been possible.

Table of Contents

Abstract iii

Acknowledgments iv

Dedication v

List of Figures ix

List of Tables xii

1. Introduction 1

2. Literature Review 5

Unidirectional Solidification 5

Rapid Solidification 6

The Ohno Continuous Caster (OCC) 10

High Strength, Two Phase Materials 12

Strengthening Mechanisms 12

Intermetallics 16

Properties of "Macrocomposites" 18

Effects of Hydrostatic Pressure on Processing 20

3. Experimental Procedure 22

Ohno Casting 22

Materials 22

Casting the Master Alloy 22

Ohno Casting 24

The Macrocomposite 25

Swaging and Drawing 26

Hydrostatic Extrusion 28
Metallography 29
Preparation for Optical Microscopy 30
Sample Preparation for the SEM 30
Sample Preparation for the TEM 31
Mechanical Properties 31
Hardness Tests 31
Compression Tests 32
Tensile Tests 32

4. Results **33**
Structure of Cast Alloys 33
Al-Fe Ohno Cast Rod 33
Al-Ni Ohno Cast Rod 34
Preparation of the Macrocomposite 37
Mechanical Properties 39
Hardness Tests 42
Large Strain Deformation 43
Al-Fe and Al-Ni Ohno Cast Materials 44
Deformation of the Al-Fe Macrocomposite 49
Fractography 51
Al-Fe Ohno Cast Alloy 51
Al-Ni Alloy Ohno cast at 769 mm/min 53
Al-Ni Alloy Ohno Cast at 524 mm/min 54
TEM Analysis of the Al_6Fe Fibers 56

5. Discussion **59**
Characterization of the Alloys 59

Mechanical Properties of the Alloys 62
The Al_6Fe Fibers 62
The Al_3Ni Fibers 65
Discussion of 5.2.1 and 5.2.2 66
Fractography 67
Wire Drawing and Hydrostatic Extrusion 68
The Al-Fe Macrocomposite 70

6. Conclusions **72**

References **74**

List of Figures

Figure 1-1 Aluminum Conductor Steel Reinforced (ACSR) 1

Figure 2-1 Phase diagram between Al and Al_3Fe 7

Figure 2-2 Dominant growth morphologies as a function of V (mm/sec) and alloy concentration 8

Figure 2-3 Phase diagram between Al and Al_3Ni 9

Figure 2-4 Effect of solidification velocity and composition on Al-Al_3Ni growth morphology 10

Figure 2-5 Ohno casting versus conventional casting 11

Figure 2-6 Schematic layout of horizontal OCC equipment 12

Figure 2-7 Relationship between proof stress and wire drawing strain 13

Figure 2-8 Data for drawn copper, silver and the copper-silver eutectic 15

Figure 2-9 Relationship between hardness and temperature for Al_3Ni and Al_6Mn 17

Figure 2-10a Influence of hydrostatic pressure on the plastic strain of Ni_3Al (taken from Zok et al. (1990)). 20

Figure 2-10b Influence of hydrostatic pressure on the effective stress at fracture (taken from Zok et al. (1990)). 21

Figure 3-1 The Al-Fe phase diagram 23

Figure 3-2 Swaging dies 26

Figure 3-3 The swaging machine 27

Figure 3-4 The wire drawing apparatus used in this study 28

Figure 3-5 Schematic of the model 06 hydrostatic extrusion apparatus 29

Figure 3-6 Schematic of the tensile test billet 32

Figure 4-1 The Al-Fe Ohno cast rod 33

Figure 4-2 The Al-Fe Ohno cast rod at a higher magnification than Figure 4-1 34

Figure 4-3 The Al-Ni alloy Ohno cast at 524 mm/min 35

Figure 4-4 Regions of Al-Al_3Ni eutectic deviating from the growth direction 35

Figure 4-5 Cross sectional view of the Al-Ni alloy Ohno cast at 769 mm/min 36

Figure 4-6 Longitudinal view of the Al-Ni Ohno cast at 769 mm/min 37

Figure 4-7 Schematic of the Macrocomposite 37

Figure 4-8 Cross section of the Al-Fe macrocomposite 38

Figure 4-9a True stress vs True strain behavior for the Al-Fe Ohno cast alloy 40

Figure 4-9b True stress vs true strain behavior for the Al-Ni alloy Ohno cast at 524 mm/min 40

Figure 4-9c True stress vs true strain behavior for the Al-Ni alloy Ohno cast at 769 mm/min 41

Figure 4-10 Kinking of the Al_6Fe Intermetallic 42

Figure 4-11 Swaged Ohno Cast Al-Fe alloy 44

Figure 4-12 Ohno cast Al-Fe drawing to a strain of 1.4. 45

Figure 4-13 Coarse Al_3Fe particles fracturing during drawing 46

Figure 4-14 Plot showing extrusion pressure vs displacement of the ram. 47

Figure 4-15 SEM micrograph of the Al-Fe OCC after hydrostatic extrusion 48

Figure 4-16 TEM micrograph of the Al-Fe OCC after hydrostatic extrusion 48

Figure 4-17 The Al-Zn-Fe bond after wire drawing 50

Figure 4-18 Effect of swaging on the hardness of the constituent materials 50

Figure 4-19a Fracture surface of the Al-Fe Ohno cast alloy 52

Figure 4-19b The Al-Fe Ohno cast alloy fracture surface at 12,000x magnification 52

Figure 4-20a Fracture surface of the Al-Ni alloy cast at 769 mm/min 53

Figure 4-20b The Al-Ni Ohno cast alloy fracture surface at 11,400x magnification 54

Figure 4-21a Fracture surface of the Al-Ni alloy Ohno cast at 524 mm/min 55

Figure 4-21b Shear bands and void growth in the Al-Ni Ohno cast alloy 55

Figure 4-21c An examination of the fracture surface and longitudinal section 56

Figure 5-1a Transverse section through the cellular structure of an Al-Al_6Fe rod eutectic (taken from Porter and Easterling (1981)) 61

Figure 5-1b The Al-Al_3Ni system studied in this project 61

List of Tables

Table 1-1 Typical strength and conductivity properties for Al conductor alloys 2

Table 2-1 Results from Cantor and Cahn showing solute trapping 7

Table 2-2 Fracture stress of various intermetallic compounds 16

Table 2-3 Hardening behavior of selected materials 19

Table 3-1 Ohno casting parameters 25

Table 3-2 Chemical compositions of Al given in weight % (from ASM Metals Handbook) 25

Table 4-1 Summary of the tensile and compression tests 39

Table 4-2 Hardness Test Results 43

Table 4-3 Allowed reflections and interplanar spacings in the Al_6Fe system. 57

1. **Introduction:**

Aluminum and it's alloys find widespread use as electrical conductors. The electrical conductivity of the best aluminum alloys lies in the range of 61 to 63 % of the International Annealed Copper Standard (IACS). The density of aluminum (2.7 g/cm^3) is much less than that of copper (8.92 g/cm^3) and as a result the specific conductivity (σ/ρ) of aluminum is much higher than that of copper. For this reason aluminum (or Al alloys) has become the material of choice for high voltage overhead transmission lines. Unfortunately, the strength of aluminum alloys is relatively low, so for this application the aluminum conductor must be reinforced by a steel core (refer to Figure 1-1) to provide the overall stiffness, strength and creep resistance required when long lengths of a conductor are suspended between transmission towers.

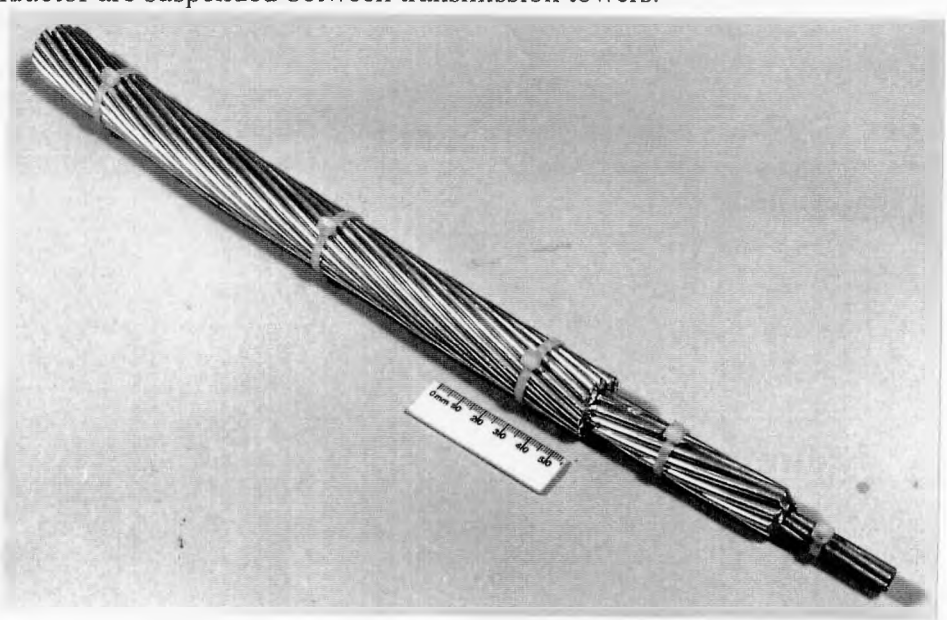

Figure 1-1 Aluminum Conductor Steel Reinforced (ACSR).

Table 1-1 (from Starke (1977)) shows some typical strength and conductivity values for current aluminum conductor alloys.

Comparison of typical properties of aluminum conductor wire

Alloy	Properties of 0 Temper (Wire)			
	TS ksi	YS ksi	Elong. in 25 cm	Conductivity (%) IACS
EC (99.6% Al)	7.45	2.75	32	63.4
Triple E (Al–0.55Fe)	9.5	6.77	33	62.5
Super T (Al–0.5Fe–0.5Co)	12.85	10.88	25	61.1
X8076 (Al–0.75Fe–0.15Mg)	10.88	6.08	22	61.5
Stabiloy (Al–0.6Fe–0.22Cu)	11.38	5.39	20	61.8
Nico (Al–0.5Ni–0.3Co)	10.88	6.77	26	61.3
X8130 (Al–0.6Fe–0.08Cu)	10.20	6.08	31	62.1

Table 1-1 Typical strength and conductivity properties for Al conductor alloys.

Many different types of "lay up" are employed in fabricating these composite conductors, but the current designs in Canada have to be quite conservative to allow for wind and ice loading during winter months and the possibility of short term excursions to 150 ^{o}C during electrical overload conditions.

The higher yield strengths for Al conductor alloys are achieved by alloying with transition elements such as iron (Fe), cobalt (Co) or nickel (Ni) (see Table 1-1). The wire is processed in such a way as to yield a microstructure of finely dispersed intermetallic phases, i.e. Al_6Fe or Al_3Ni, which helps to stabilize the fine grain structure. This

microstructure, coupled with very low solid solubility of transition elements in aluminum at room temperature, leads to excellent room temperature conductivity.

In the past, two approaches have been taken in the development of high strength wires for their use as overhead transmission lines. In the first approach a reinforcing agent such as high strength steel, is used to increase the overall strength. By using this approach, any increase in resistivity can be minimized while maintaining sufficient strength levels. The second approach is to develop a composite conductor, in situ or macrocomposite, that exhibits both adequate strength and conductivity. This approach has been taken up in the development of high strength, high conductivity Cu wires for use in high field magnets. This has been the subject of a recent Ph.D. thesis at McMaster (Wood (1994)). In this study, ultra drawn copper alloys (Cu-Ag and Cu-Nb) have been the material of choice. Through co-deformation of these two phase materials via drawing, sufficient strength and conductivity were achieved.

The present research project arose from this earlier study of Cu alloys. The objective was to create a two phase aluminum alloy, where the two phases would co-deform on drawing. As in the case of ultra drawn copper alloys, if co-deformation occurs, very high strengths might be achieved for these aluminum alloys. Another approach explored in this work was the development of a macroscopic composite. This has been demonstrated recently in the copper system by combining Cu and steel, followed by drawing the two phase mixture. However, for aluminum the macroscopic composite produced was made from aluminum and iron. The rationale behind choosing

these materials for the aluminum macrocomposite was to choose two materials which had similar yield strengths so that the materials would co-deform easily when drawn. The materials of choice for the two phase alloys were Al-Fe and Al-Ni. These were chosen primarily because there is a eutectic reaction at the aluminum rich side of the phase diagram and Fe and Ni both have very low solid solubilities in Al at room temperature. Thus, this approach should minimize any increase in resistivity due to solute.

The overall goal of this thesis was to explore the co-deformation of two phase aluminum alloys for their potential use as a high strength, high conductivity wire.

2. Literature Review

The overall objective of this thesis was to explore the methods of fabrication and microstructural development of a high strength, high conductivity aluminum alloy. In this study, two approaches have been taken. First, the development of fine scale, two phase materials produced by directional solidification and subsequently cold drawing was considered. In addition, a "macrocomposite" which combined aluminum with an embedded phase, which had a higher work hardening rate, was developed. For clarity, the literature review will deal with the following list of topics: (1) The influence of solidification rate on microstructure, (2) unidirectional solidification, including Ohno casting and (3) a review of high strength two phase materials and their application for cases which require a combination of high strength and high conductivity.

2.1 Unidirectional Solidification

Work done on unidirectional and rapid solidification of the Al-Fe and Al-Ni eutectics will be reviewed in this section. Hughes and Jones (1976) were able to produce a "microstructure selection map" (showing the relationship between the phases produced over a range of solidification rates and alloy composition) for the Al-Fe system while Barclay et al. (1971) established the effect of growth rate and composition on microstructural development in the Al-Ni system. The essential results from the work on these systems display that non equilibrium phases and microstructures are evident when high solidification rates are present. Using this background knowledge, the selection of

solidification rates in the Ohno Continuous Caster (OCC), which combines both rapid and unidirectional solidification was made in an attempt to develop improved properties in the as cast condition as compared to conventionally cast materials.

2.1.1 Rapid Solidification

The constitutional and microstructural advantages to be gained from rapid solidification have been used to develop improved structural alloys from crystalline materials and enhanced mechanical, chemical, electrical and magnetic properties in amorphous alloys (Froes and Carbonara (1988)). The near net shape characteristics of many of these products and the special properties which result from rapid solidification make them very attractive for industrial applications. The influence of rapid solidification can be summarized in four effects: a) refinement of the scale of the structure, b) modification of the phase diagram, c) the production of new non-equilibrium phases, and d) trapping of solute resulting in ranges of solid solution.

In rapid solidification processing a great variety of phases and microstructures may form, which are not predicted from equilibrium phase diagrams. (Kurz and Gilgen (1994)) For a better understanding and control of the solidification behavior of alloys, the experimental approach has been and is still of great importance in this field. In a study by Cantor and Cahn (1976), the extent of solute trapping which has resulted from rapid solidification was identified. Table 2-1 summarizes the results obtained by Cantor and Cahn in a study of Al alloys and compares the equilibrium solid solubility and the solubility when the alloy has been rapidly quenched from the liquid.

		Maximum Solid Solubility (at%)			
Solvent	Solute	equilibrium	sputtered	liquid-quenched	thermally evaporated
Al	Cu	2.5	28.5	18.0[7]	–
Al	Ni	0.02	20.9	7.7[8]	11.5[10]
Al	Fe	0.026	12.9	4.4[9]	7.5[11]
Ni	Al	21.0	16.2	–	–

Table 2-1 Results from Cantor and Cahn showing solute trapping.

Work done by Hughes and Jones on the Al-Fe system using rapid solidification has also yielded some interesting results. Figure 2-1 shows the Al-Al_3Fe phase diagram. The eutectic between these two phases is located at 1.9 wt% Fe. However utilizing rapid solidification rates, different morphologies and phases have been found. Figure 2-2 (from Hughes and Jones (1976)) illustrates the effect that solidification speed and wt% Fe in Al has on the phases that form in the alloy. The diagram in Figure 2-2 has been termed a "microstructure selection map" which shows the phases formed and the scale of these phases as a function of the solidification rate.

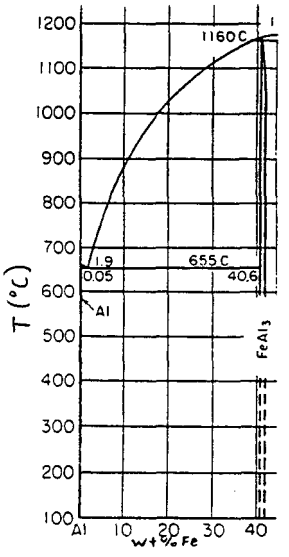

Figure 2-1 Phase diagram between Al and Al_3Fe.

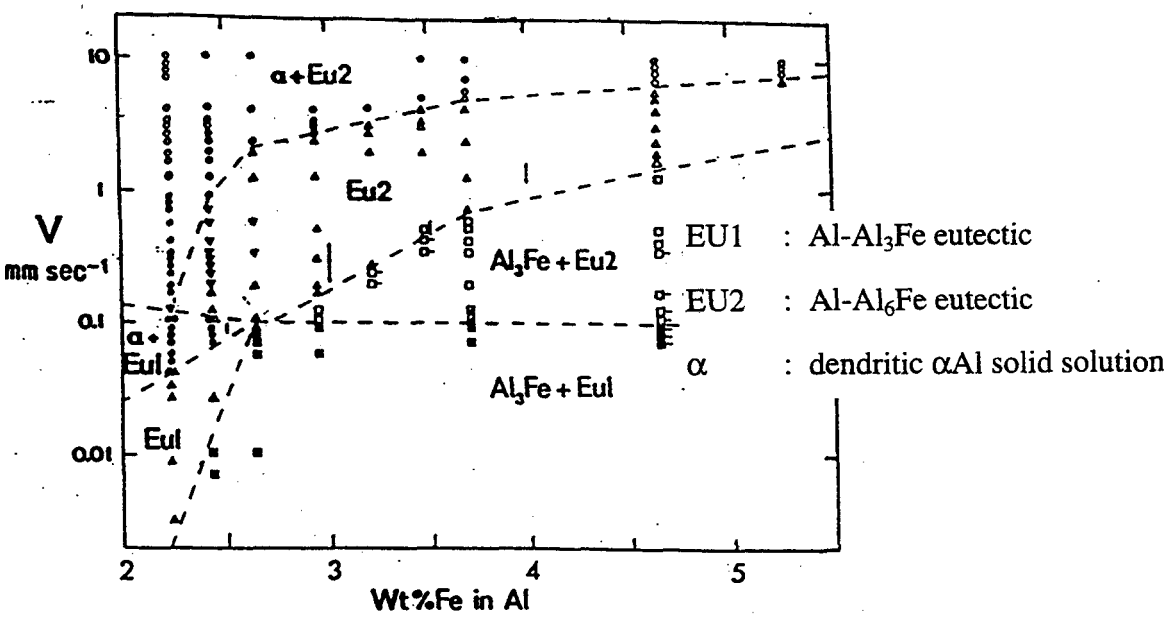

Figure 2-2 Dominant growth morphologies as a function of V(mm/sec) and alloy concentration.

At the eutectic composition, depending on the solidification velocity, there are three different growth morphologies that can be observed. It is also interesting to note that a metastable phase, Al_6Fe, forms under certain solidification conditions.

The phase diagram for the Al-Al_3Ni eutectic system is shown in Figure 2-3. It is apparent from the work done by Barczy et al. (1993) that no metastable phases are formed during eutectic solidification of Al and Al_3Ni. However, rapid solidification does influence the morphology of the structure. Barclay et al. illustrated this in work done on the Al-Al_3Ni system. (refer to Figure 2-4) A fully eutectic structure can be produced in excess of the eutectic composition by solidifying the melt at faster rates. These studies have helped to identify the morphology present in the solidified structure. Moreover, studies on solidification have shown that the spacing of the eutectic can be described by equation 2.1 where v is the solidification velocity and λ is the eutectic spacing. Therefore, for any system, the value on the right hand side of equation 2.1(constant)

remains constant while v and λ vary. This is why faster solidification rates lead to a refined structure.

$$v\lambda^2 = constant \tag{2.1}$$

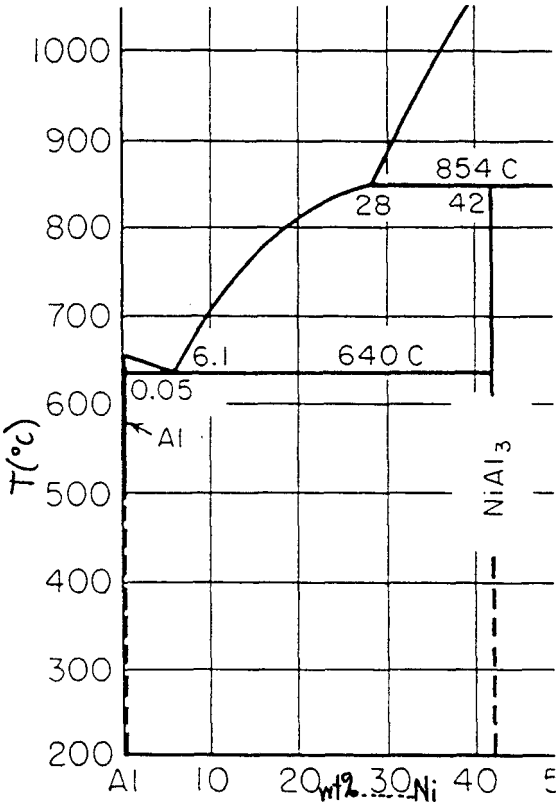

Figure 2-3 Phase diagram between Al and Al_3Ni.

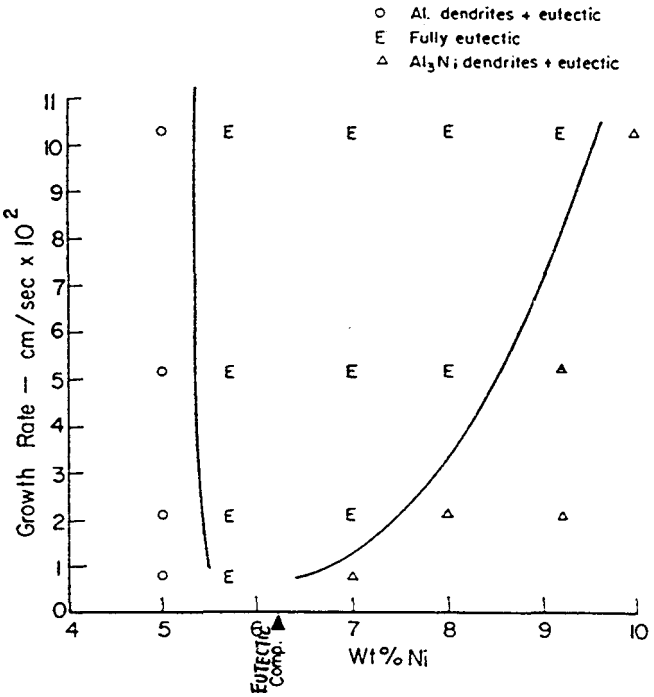

Figure 2-4 Effect of solidification velocity and composition on Al-Al_3Ni growth morphology.

Therefore, it is apparent that one cannot base the development of an alloy on equilibrium phase diagram considerations only. For the Al-Fe and Al-Ni systems, it has been shown that different morphologies can form at different solidification rates. Thus, "microstructure selection maps" can play a useful role in the development of the end product.

2.1.2 The Ohno Continuous Caster (OCC)

The OCC process, invented by Professor A. Ohno of The Chiba Institute of Technology, is a novel casting technique used to achieve special cast structures with unique properties. The features include a distinctive ability to produce a single crystal or

unidirectional columnar grains, a remarkably clean cast surface without witness marks and in many cases an alloy having extremely good ductility.

As shown in Figure 2-5, the key feature which differentiates the OCC process from conventional casting techniques is the delivery of molten metal into a heated mold, the temperature of which is held just above the solidification temperature of the metal to be cast.

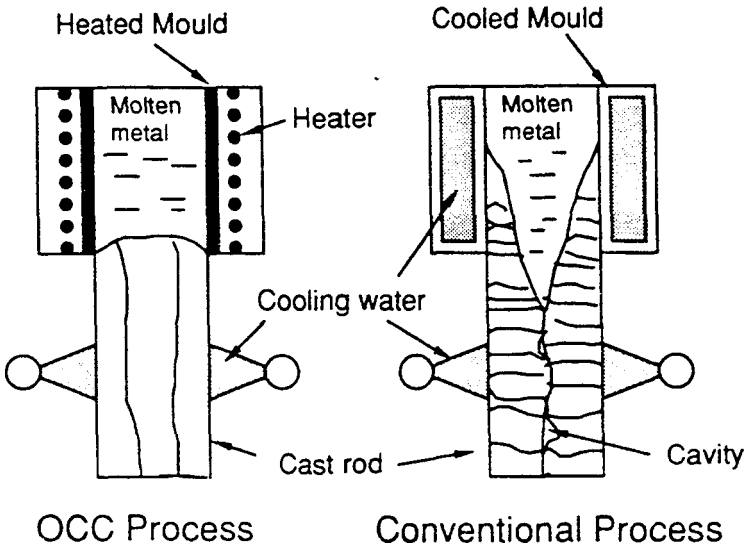

Figure 2-5 Ohno casting versus conventional casting.

The OCC can cast low melting point materials at speeds of up to 1 meter per minute (m/min). Typically, larger diameter materials (~ 8mm dia.) cannot be cast at such speeds because of the instabilities that exist during casting such as vibrations from the surroundings or fluctuations in the mold temperature. Thus, breakout will occur causing the casting process to be aborted. Figure 2-6 (from Soda et. al. (1995)) shows a schematic diagram of the experimental setup of the OCC. The level control block controls the head of metal during casting. The molten metal is delivered through a heated mold where the heat flow is parallel to the casting direction. This molten metal is solidified by use of cooling water sprays ranging from 10 to 20 mm from the mold exit. The end product, a net shape cast rod, is continuously withdrawn by a set of pinch rolls.

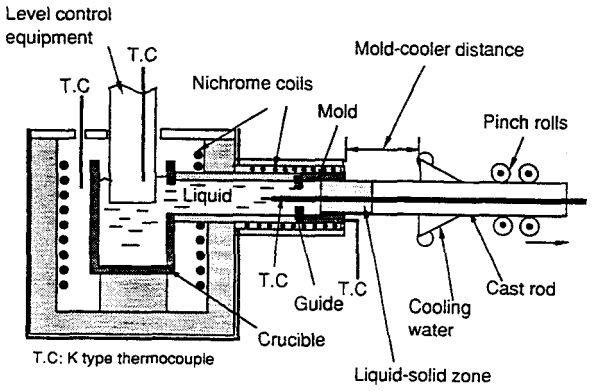

Figure 2-6 Schematic layout of the horizontal OCC equipment.

2.2 High Strength, Two Phase Materials

2.2.1 Strengthening Mechanisms

The preceding section dealt with the dependence of morphology and scale of structures on the solidification processes. In this section work concerned on the strengthening of two phase materials will be reviewed with emphasis on how the deformation of materials leads to high strength. A much more detailed review of deformation of two phase materials can be found in the work of G. Sevillano (1981).

It is useful to begin by considering the processing of high strength wires, such as Fe-Fe_3C. High strength steel wires are made from steel of eutectoid composition which has previously been austenitized and transformed to fine pearlite or upper bainite at about 500 °C. This material is subsequently cold drawn in a series of draw steps; the strength of the wire increases with increasing reduction in area. A relationship was proposed by Embury and Fisher (1966) to relate the scale of the microstructure after large plastic strains to strength levels for drawn pearlite. This strengthening mechanism was assumed

to be dependent upon the spacing of the cell walls which acted as boundaries to dislocation motion. These cell walls consist of continuously deformed cementite plates, complex arrangements of dislocations and fragmented carbides. These cell walls were assumed to be barriers responsible for strengthening in a manner analogous to that associated with the Hall-Petch relationship (Hall (1951) and Petch (1953)). The strength of the drawn steel wires was described by the equation:

$$\sigma_y = \sigma_o + \frac{k}{\sqrt{d}} \exp(\varepsilon/4) \qquad \textbf{(2.2)}$$

where σ_y is the proof stress, σ_0 is the friction stress of the matrix, k is the Hall-Petch slope, d is the initial barrier spacing(prior to drawing) and ε is the true drawing strain. The data obtained by Embury and Fisher from an investigation of drawn steel (patented) wires is shown in Figure 2-7.

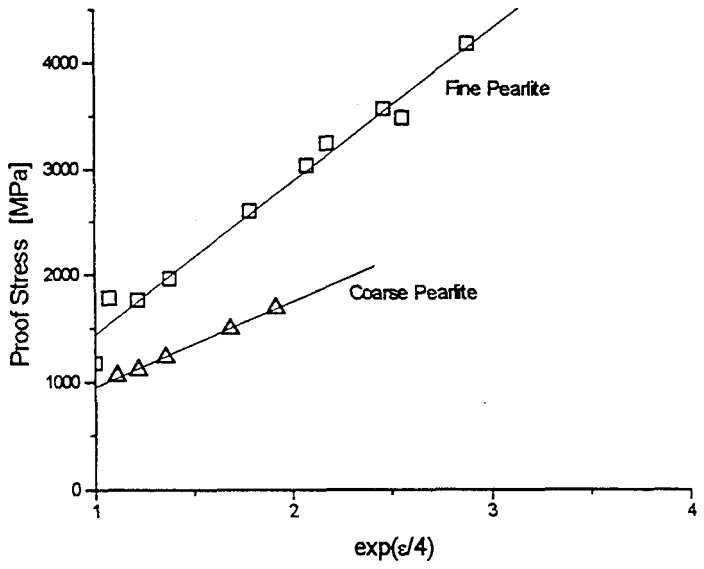

Figure 2-7 Relationship between proof stress and wire drawing strain.

The relationship described by equation 2.2 shows that in order to maximize the strength of the wire, one would need to minimize the initial spacing of the second phase (d_o) and deform the material to high strains (maximize ε).

This model has also been used for Cu-Ag alloys (Frommeyer and Wasserman (1975)) and Cu-Nb alloys (Wood (1994)). In steel, the pearlite consists of alternating layers of cementite embedded in a ferrite matrix (Fe-Fe_3C). Upon deformation of this structure, the Fe and Fe_3C undergo extensive co-deformation although some of the cementite particles were observed to fragment during drawing. It is through this process of co-deformation that the wire draws it's strength. Frommeyer and Wasserman (1975) and Berk et. al. first demonstrated that when these materials were drawn to very high strains, tensile strengths of about 1.5 GPa or more could be reached. It is worthwhile to compare the strengths of these drawn composite wires with maximum strengths which can be achieved by drawing the individual components to equivalent strains. Data from Frommeyer and Wasserman is shown in Figure 2-8, and is typical of the general behavior of most fine scale, two phase systems and their bulk constituents after deformation. In the Cu-Ag and Cu-Nb systems, there is co-deformation between the constituent phases, as both phases are sufficiently ductile to flow plastically during drawing. Equation 2.2 provides a sound basis for explaining the strengthening of the Fe-Fe_3C system but not necessarily for the Cu-Nb and Cu-Ag systems.

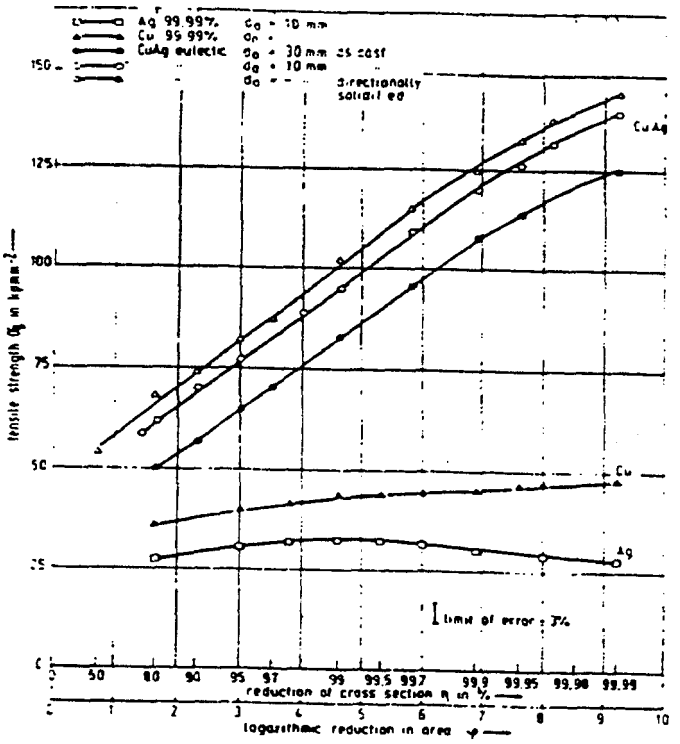

Figure 2-8 Data for drawn copper, silver and the copper-silver eutectic.

Strengths associated with the drawing of either pure Cu, Nb or Ag saturate at very low stresses (400-500 MPa). By combining these materials and drawing them to high strains, strength levels of up to 1.5 GPa have been achieved. Two possible explanations were proposed by Wood (1994) in an attempt to describe the origin of the strengths. Both explanations are based on the premise that there is an increased storage of energy which can be directly related to the high strength.

In order for co-deformation of two phases to be viable, several basic criteria must be met. The materials being deformed must have sufficient slip systems, have a relatively simple crystal structure and have similar yield strengths. Copper, silver and niobium all meet these criteria. These properties enable alloys to co-deform to large plastic strains without great difficulty and achieve high strengths.

2.2.2 Intermetallics

In the previous section, some of the conditions that must be met in order to obtain co-deformation between two phases were discussed. In this section, the properties of intermetallics, namely Al_6Fe, Al_6Mn and Al_3Ni will be reviewed. Some mechanical properties of these intermetallic compounds will be presented to try and predict if co-deformation between these intermetallics and a ductile material can be accomplished.

Most intermetallics are inherently brittle, i.e. they will not deform extensively by plastic flow before fracture. This has been shown for the Al_3Ni phase by Hertzberg et. al. (1965). In this study, Al_3Ni fibers were extracted from an Al matrix and pulled in tension in a micro tensile testing apparatus. The fiber failed in a brittle manner and the resulting fracture stress of the fiber is shown in Table 2-2. The fracture stress of Al_6Fe has not been measured but an estimate can be made by comparing it to the Al_6Mn phase. In this review, the value of the fracture stress shown in Table 2-2 for Al_6Mn will be used as an estimate for the fracture stress of Al_6Fe since Al_6Fe and Al_6Mn are isomorphous. The reason that no information is available for Al_6Fe is because it is a metastable phase and is only found in alloys after rapid solidification.

Material	Fracture Stress (MPa)	Reference
Al_3Ni	2200	Hertzberg et. al. (1965)
Al_6Mn	2000	Westbrook et. al. (1994)
Al_6Fe	N/A	

Table 2-2 Fracture stress of various intermetallic compounds.

Another useful piece of information with respect to intermetallics is how their mechanical properties vary with temperature. Figure 2-9 is a reproduction from Petty (1961) showing the relationship between hardness and temperature for Al_6Mn and Al_3Ni.

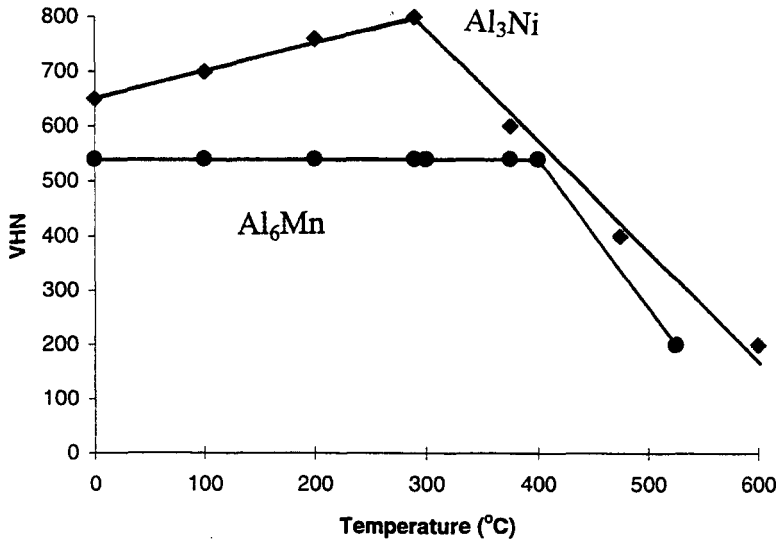

Figure 2-9 Relationship between hardness and temperature for Al_3Ni and Al_6Mn.

Reviewing the information presented in Figure 2-9 leads to an interesting conclusion. The yield strength of the constituent phases presented in the previous section (i.e. Cu and Nb or Cu and Ag) differ at most by approximately a factor of four. However, the difference between the yield strength of Al and the strength at which any deformation will occur in the intermetallics (Al_6Fe or Al_6Mn) is an order of magnitude greater. Therefore, co-deformation may be much more difficult to achieve when working with the Al-Al_6Fe or Al-Al_3Ni systems as compared to the Cu-Nb or Cu-Ag systems. Figure 2-9 shows at what temperature the intermetallic becomes more ductile. The temperature where the slope of the line changes drastically is called the inflection temperature (T_i).

Below T_i, only limited plastic deformation, if any, occurs by slip while above T_i diffusion controlled processes such as dislocation climb and grain boundary sliding prevail. It has been found by Rohatgi et al. (1987) that the Al_3Ni fibers break up during deformation at ambient temperatures. Therefore, co-deformation at temperatures > T_i might be possible.

2.2.3 Properties of "Macrocomposites"

The term "macrocomposite" refers to a composite which derives its strength from constituents dispersed on a macro scale instead of on a micro scale. The *in situ* composites discussed earlier depend on constituents dispersed that are on the scale of micrometers (μm) or nanometers (nm). A "macrocomposite" has a strengthening constituent dispersed on the scale of mm.

"Macrocomposites" have been produced in the past using many different combinations of materials but one of particular interest to this study was that created by Zhou et al. (1995) using Cu and steel as the two constituents. Zhou was able to successfully combine and draw both Cu/carbon steel and Cu/stainless steel composites which were approximately 8 mm in diameter to strengths in excess of 1 GPa. There were two designs, both of which used a Nb foil wrapped around the steel. The Nb acted as a diffusion barrier between the steel and copper. The first design called for a steel core to be embedded in a Cu can while the second design used a steel tube surrounded by a Cu core and Cu can. The resulting billets were put through several cold working operations and heat treatments in order to combine the constituent phases. The strengthening mechanism at work during the drawing operation can be described by equation 2.3 which is an empirical relationship based on a rule of mixtures. Therefore, the overall strength of the composite will be determined by the following equation:

$$\sigma_{composite} = V_{Cu}\sigma_{Cu} + V_{Steel}\sigma(\varepsilon)_{Steel} \qquad (2.3)$$

where $\sigma_{composite}$, σ_{Cu} are the tensile strengths of the composite and Cu respectively, V_{Cu} and V_{Steel} are the volume fractions of the Cu and steel phase respectively and $\sigma(\varepsilon)_{Steel}$ is the strength of the steel as a function of strain (which can be found in Table 2-3).

Could an Al/steel or Al/Fe "macrocomposite" be created and drawn to achieve similar strengths? As long as there is a good bond between the two phases, one would assume that this goal might be met. The following table lists the strengths can be achieved for different materials as a function of strain[$\sigma(\varepsilon)$].

This table is useful in helping one predict what strengths can be achieved if a certain amount of wire drawing strain can be imposed on a material. Once the strengths are known, one can use the simple rule of mixtures approach shown in equation 2.3 to determine the overall strength of the composite.

Material	Hardening Behavior [$\sigma(\varepsilon)$] (σ in MPa)	Reference
Fine pearlite	$\sigma_y = 11 + 1430\exp(\varepsilon/4)$ [0<ε<4.25]	Embury and Fisher (1966)
Coarse pearlite	$\sigma_y = 163 + 790\exp(\varepsilon/4)$ [0<ε<2]	Embury and Fisher (1966)
301 Stainless Steel	$\sigma_{UTS} = 316\varepsilon^{0.189}$ [0<ε<10]	Llewellyn and Murray (1964)
Pure Cu	$\sigma_{UTS} = 98 + 142\ \varepsilon$ [0<ε<0.7]	Frommeyer and Wasserman (1975)
Pure Fe*	$\sigma_y = 234 + 153\varepsilon$ [0<ε<7]	Langford and Cohen (1975)
Pure Al	$\sigma_y = 50 + 41\varepsilon$ [0<ε<3]	Gil Sevillano (1981)

* The Fe used in this study had 0.007 wt% C and the relationship stated does not apply for [0<ε<0.5]. The flow stress at ε=0 is approximately 100 MPa.

Table 2-3 Hardening behavior of selected materials.

2.3 Effects of Hydrostatic Pressure on Processing

It is well known that the stress state can affect damage and fracture during plastic straining. Imposing hydrostatic pressure on a material can help suppress damage and prolong the deformation of an inherently brittle material (this has been shown by Brownrigg et al. (1983)). Zok and Embury (1990) have shown that for Ni_3Al, the strain to fracture and fracture stress increase linearly with the level of hydrostatic pressure applied to the material. Figure 2-10a and 2-10b shows how the fracture strain and fracture stress are affected by testing Ni_3Al in the presence of a superimposed hydrostatic stress.

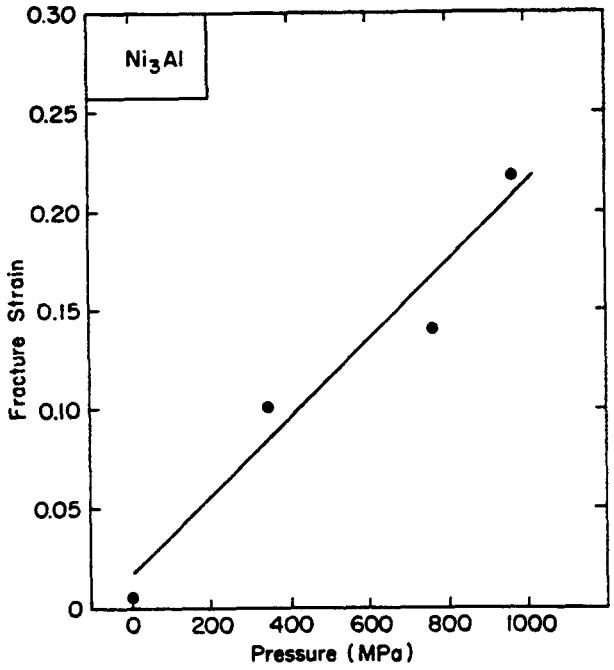

Figure 2-10a Influence of hydrostatic pressure on the plastic strain of Ni_3Al (taken from Zok et al.(1990)).

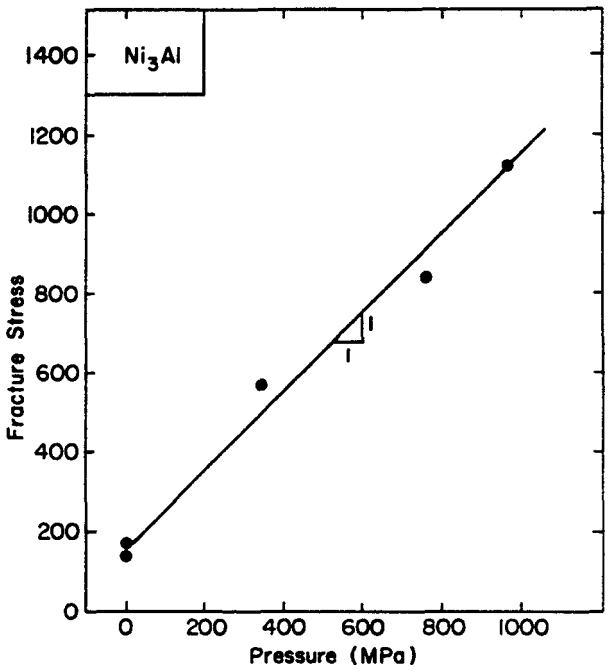

Figure 2-10b Influence of hydrostatic pressure on the effective stress at fracture (taken from Zok et al. (1990)).

3. Experimental Procedure

The following section will outline the different experimental techniques used for creating and preparing samples for experiments and analysis.

3.1 Ohno Casting

3.1.1 Materials

Ultra high purity aluminum (99.999%) was provided by The Alcan Research and Development Centre courtesy of Dr. G. Burger. This material was used for the casting of the OCC Al rod. It was received in the form of pieces which had been cut from an ingot. The Fe was electrolytic grade (from A.D. Mackay Ltd.) and was 99.95% pure. The analysis of residual elements in the Fe was not available. The material for the Al-Ni cast was obtained from Alcan in ingot form and contained approximately 5.7 wt% Ni. It was used directly in the Ohno process.

3.1.2 Casting the Master Alloy

The Al-Fe master alloy was prepared in ingot form weighing approximately 2 kilograms (kg). In order to explain the method used for alloy fabrication, it is useful to refer to the Al-Fe phase diagram in Figure 3-1.

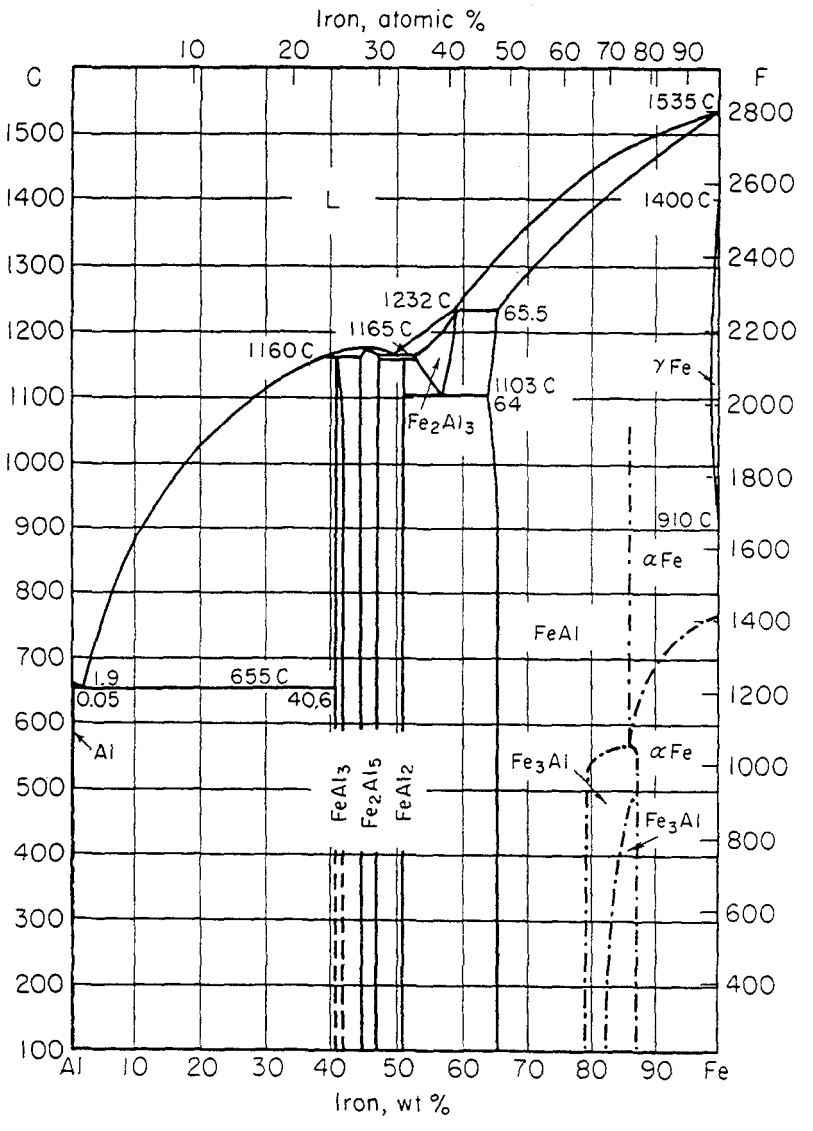

Figure 3-1 The Al-Fe phase diagram.

The melting points of pure Fe and Al are 1535 °C and 660 °C respectively. One way to reduce the difficulties associated with the difference between the elements was first to produce Al_3Fe pieces which have a melting point of 1160 °C. The Al_3Fe was produced by arc melting in a 0.5 atmosphere (atm.) of Argon (Ar). The 2 kg Al-Fe

master alloy was then produced by adding the Al and Al_3Fe to an alumina crucible and melting by induction heating under 0.5 atm. Ar. Before the constituents were added, the crucible was sprayed with Boron Nitride (BN) to prevent the melt from wetting the sides and bottom of the crucible. The peak temperature of the melt was estimated to be 1200 ^{o}C using an optical pyrometer. The melt was held at this temperature for approximately five hours before casting.

3.1.3 Ohno Casting

The experimental procedure for Ohno casting can best be appreciated by reference to Figure 2.6. The material to be cast was placed inside the crucible and heated to a temperature approximately 10 to 20^{o}C above the melting point. Once the material was molten, the melt was stirred with an alumina rod which had been preheated to the melt temperature. A steel dummy rod was placed at the exit of the mold to provide a means of starting the casting process. The mold was also preheated to a temperature just above the melting point of the material. With all of the heating conditions established, the cooling water was turned on and impinged on the steel rod approximately 20 mm from the mold exit point. The level control block was then lowered and pinch rolls engaged to initiate casting. The exact conditions held during casting are listed in Table 3-1. The casting rate of the rod was slow at the start to allow for the low thermal conductivity of the steel dummy rod. Once the cooling water contacted the Al, steady state conditions were established.

Material	Diameter of Cast Rod (mm)	Casting Speed (mm/min)	Mold Exit Temp. (°C)	Mold Cooler Distance (mm)
Al-Fe	8	85	665	22
Al-Ni #1	4	524	665	20
Al-Ni #2	4	769	665	18

Table 3-1 Ohno casting parameters.

3.2 The Macrocomposite

The macrocomposite was produced at a later stage in the research program. The macrocomposite was fabricated from pure aluminum and iron. Chemical composition limits are listed in Table 3-2 for the Al. The Fe was analyzed for carbon content and was found to contain less than 0.005 wt% (no other data was available).

Al	Si	Fe	Cu	Mn	Cr	Zn	Ga	V+Ti	B	others
99.50 min	0.10 max	0.40 max	0.05 max	0.01 max	0.01 max	0.05 max	0.03 max	0.02 max	0.05 max	0.03 max

Table 3-2 Chemical Compositions of Al given in weight % (from ASM Metals Handbook).

A 4.4 mm dia. hole was drilled into the Al rod so that the Fe rod could be embedded into the Al. The Fe rod was approximately 4.0 mm in diameter. The first

attempt to combine the Al and Fe was done using pure Fe and pure Al and swaging the two together. In the second attempt, to prevent the formation of any intermetallics between the Al and Fe, the Fe rod was galvanized. The Fe rod was dipped into a molten bath of zinc (Zn) held at 440°C and allowed to sit in the zinc bath for five minutes. As a result, a thin uniform coating of Zn was left on the Fe and the Zn coating acted as a barrier layer for the Al and helped to promote adhesion of the two metals during drawing.

3.3 Swaging and Drawing

To begin this section it is worthwhile to refer to Figures 3-2 and 3-3 so the swaging operation can be fully understood. Figure 3-2 shows the two swaging dies used in the rotary swaging operation. Figure 3-3 shows the front face of the swager, illustrating how the swaging dies fit into the machine.

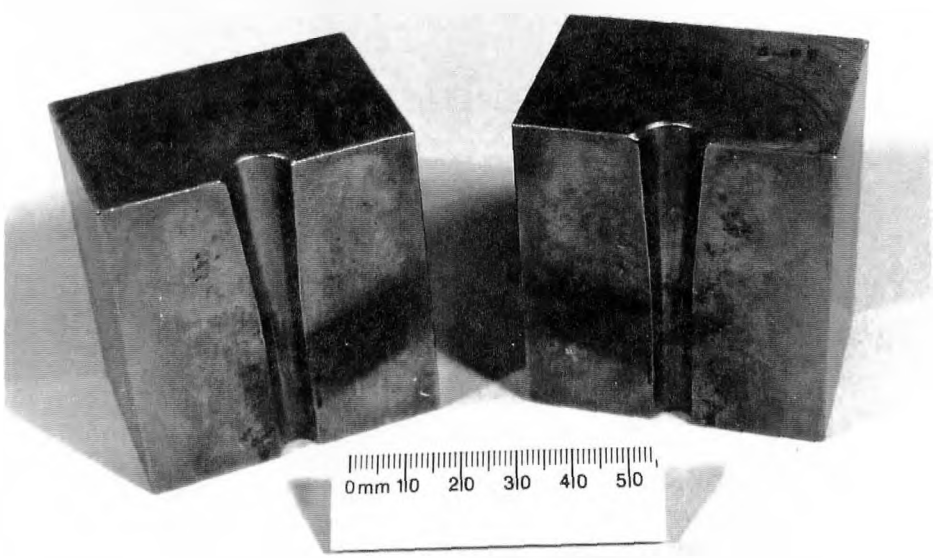

Figure 3-2 Swaging dies.

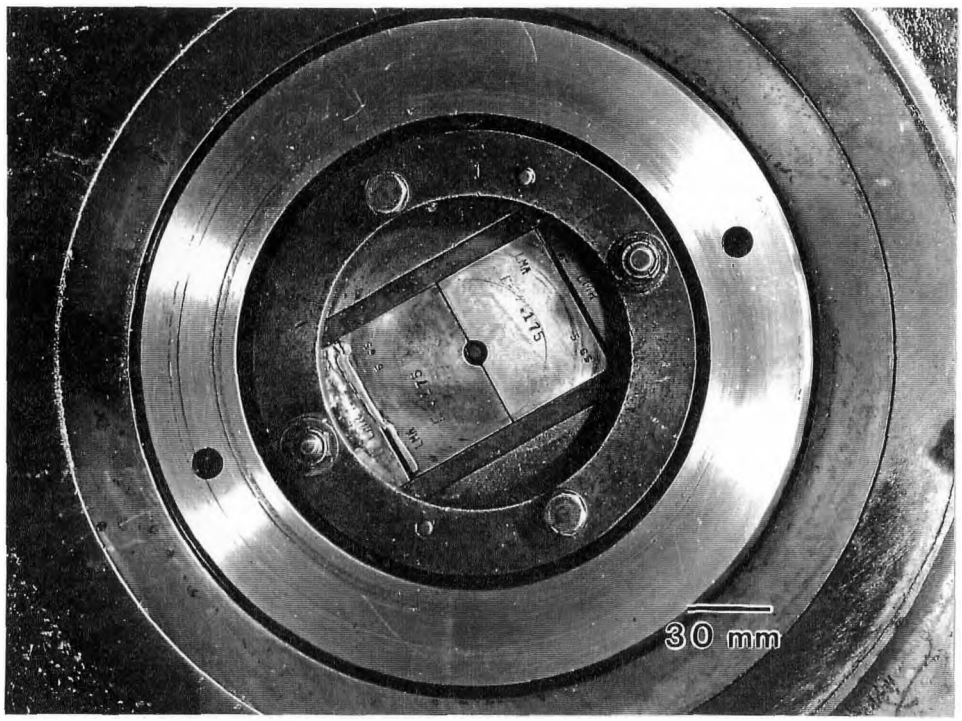

Figure 3-3 The Swaging machine.

The swaging machine used in this study was a Fenn Rotary Swager. Swaging was used as a preliminary process to reduce the diameter of a rod or wire prior to drawing. The next step in the deformation of the Al wire was wire drawing. After swaging, the wire was placed through the wire drawing die and gripped via a jaw grip on the Lloyd's tensile machine. The wire drawing was performed in a small scale wire drawing apparatus shown in Figure 3-4. This experimental setup enables the user to draw wire up to lengths of one meter. The draw speed was 25 mm/min and the lubricant (supplied by Magus Chemical) was Cal-64. This lubricant was used to reduce the friction between the die and the wire. The amount of deformation per pass corresponded approximately to a true strain of 0.2.

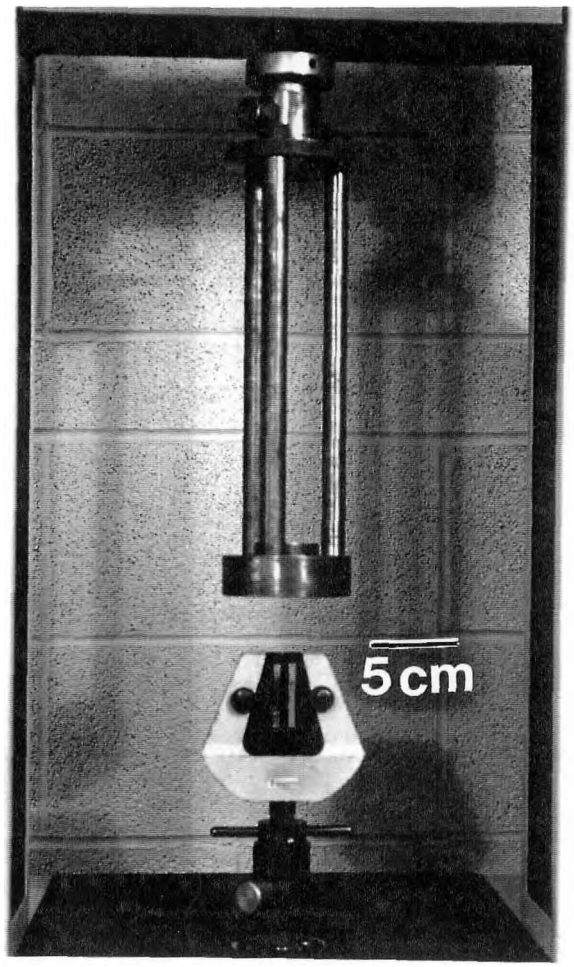

Figure 3-4 The wire drawing apparatus used in this study.

3.4 Hydrostatic Extrusion

Material taken from the as cast alloys was machined into billets for hydrostatic extrusion. A schematic of the hydrostatic apparatus is shown in Figure 3-5. The billet was placed into the top chamber (marked A) and allowed to sit in a die which separated the upper and lower chambers. The chambers were sealed off and filled with fluid. The pressure in the top chamber, P_T, increased until the billet started to extrude. The billet entered the bottom chamber (marked B) at a pressure, P_B, equal to 0.75 P_T. Once

extrusion was completed, the pressure was released and the sample taken out. The billets were machined to exactly fit the profile of extrusion die so as to eliminate as much redundant work as possible.

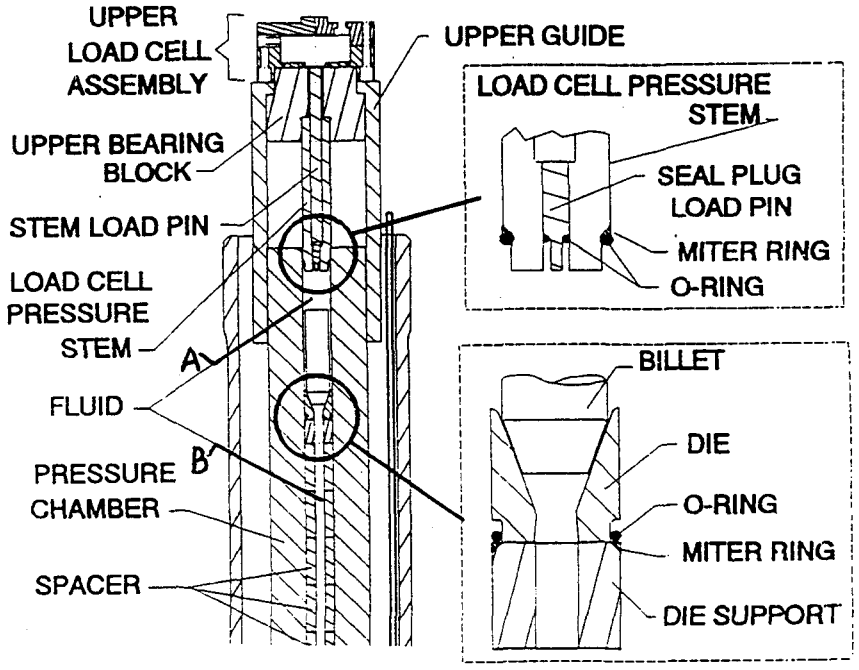

Figure 3-5 Schematic of the model 06 hydrostatic extrusion apparatus.

3.5 Metallography

The following section is centered on the experimental techniques used to prepare samples.

3.5.1 Preparation for Optical Microscopy

All samples were mounted in lucite, allowed to cool and then ground. The abrasive papers used were 200, 400, 600 and 800 grit SiC. They were used in this particular order and used until all scratches introduced from the previous paper disappeared. The sample was then cleaned with methanol and wiped with cotton to remove any contamination from the surface before polishing. After cleaning, the samples were polished with a 6 μm diamond paste, cleaned, polished with a 1 μm diamond paste, cleaned and finally polished with a 0.3 μm Al_2O_3 suspension and cleaned. At this point, all of the scratches would normally have been eliminated. The etchant used for these alloys was a 5% NaOH solution. After etching for 10 seconds, the samples were washed and dried prior to optical microscopy.

3.5.2 Sample Preparation for the SEM

The samples that were prepared for analysis in the SEM were initially mounted, ground, polished and etched as outlined in 3.5.1. The samples had to be removed from the lucite mold by cutting away as much lucite as possible and placing the sample plus remaining lucite in dichloromethane, to dissolve the lucite. Evaporation was minimized by covering the container with tin foil. Cleaning the sample was done in two steps; an ultrasonic wash in acetone followed by an ultrasonic wash in methanol. Total time of immersion in the two liquids was approximately five minutes. After drying the sample, it was ready for examination in the Phillips 515 SEM.

3.5.3 Sample preparation for the TEM

The first step in preparation of the material for TEM was cutting off 300 μm thick slices using a spark cutter. Discs approximately 3 mm in diameter were then spark cut from the slices. These discs were ground down to 130 μm with a polishing jig. Careful attention was paid to make sure that both surfaces were evenly ground. The paper used was 600 grit SiC. Once a thickness of 130 μm was reached, both sides were polished with a 1 μm diamond paste until a lustrous finish appeared on each face. The sample was then ready for dimpling.

The sample was placed on a small cylindrical mount and secured with a piece of wax. This mount was placed on the dimpler and the sample was dimpled to leave a thickness of 30 μm. The sample was then polished with a 1 μm diamond paste again until a lustrous finish appeared on the surface. The final step was to perforate the sample. This was done by placing it in an ion-beam thinning device using 4 kV, Ar ions and a current of 0.3 mA.

3.6 Mechanical Properties

3.6.1 Hardness Tests

All hardness tests were performed with a Vicker's Hardness Indenter. Samples were placed onto a stage where a diamond indenter was depressed onto the sample with either a 25 or 50 gram load, depending on the hardness of the material. The load was depressed onto the sample for 15 seconds after which the size of the identation was recorded and a value of Vicker's Hardness Number (VHN) was calculated.

3.6.2 Compression Tests

Billets were machined having dimensions of 7 mm diameter and a length of 10 mm. Teflon tape was placed on both surfaces of the billet to reduce friction between the billet and the dies. The crosshead on the Lloyd's machine was programmed to run at 2 mm/min.

3.6.3 Tensile Tests

Billets were machined with dimensions shown in Figure 3-6. These billets were designed to fit a specific set of dies for the MTS tensile testing machine. The extension was measured by means of an extensometer and the load was automatically monitored by the MTS machine.

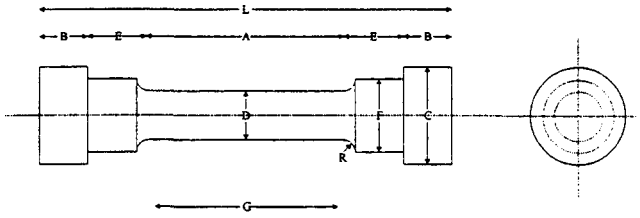

DIMENSIONS

A - LENGTH OF REDUCED SECTION - 0.625 + 0.005 in.
B - LENGTH OF END SECTION - 0.139 +/- 0.005 in.
C - DIAMETER OF END SECTION - 0.198 +/- 0.002 in.
D - DIAMETER - 0.113 +/- 0.002 in.
E - LENGTH OF SHOULDER AND FILLET - 0.208 +/- 0.005 in.
F - DIAMETER OF SHOULDER - 0.141 +/- 0.002 in.
G - GAGE LENGTH - 0.450 +/- 0.005 in.
L - OVERALL LENGTH - 1.319 +/- 0.005 in.
R - RADIUS OF FILLET - 3/32 in.
SURFACE ROUGHNESS : EQUIVALENT TO 800 GRIT OR AS GOOD AS I

Figure 3-6 Schematic of the tensile test billet.

4. Results

4.1 Structure of Cast Alloys

4.1.1 Al-Fe Ohno Cast Rod

The Al-Fe Ohno cast rod contained 2.0 wt % Fe and was cast at a speed of 85 mm/min. The directionally solidified microstructure shown in Figure 4-1 and 4-2 consists of primary aluminum dendrites surrounded by the Al-Al_6Fe eutectic with an Al_6Fe rod morphology. The diameter of the rods are in the range of 150 to 200 nm with a spacing of approximately 400 to 500 nm. It is important to note (Figure 4-2) that the degree of misalignment of the rods with respect to the growth direction was approximately $\pm 25^{o}$; indicating that the Ohno caster does not provide 100% directional solidification.

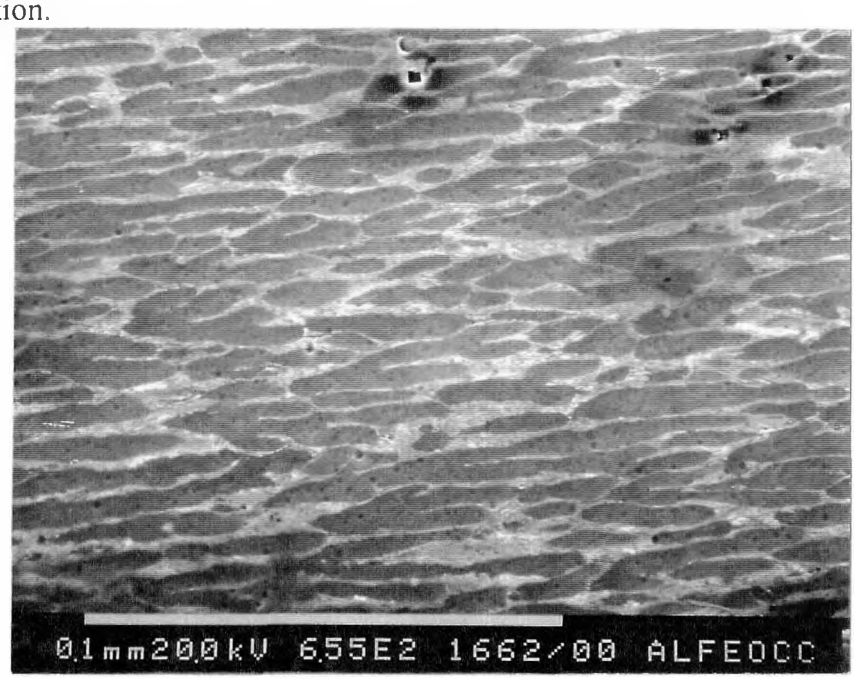

Figure 4-1 The Al-Fe Ohno cast rod.

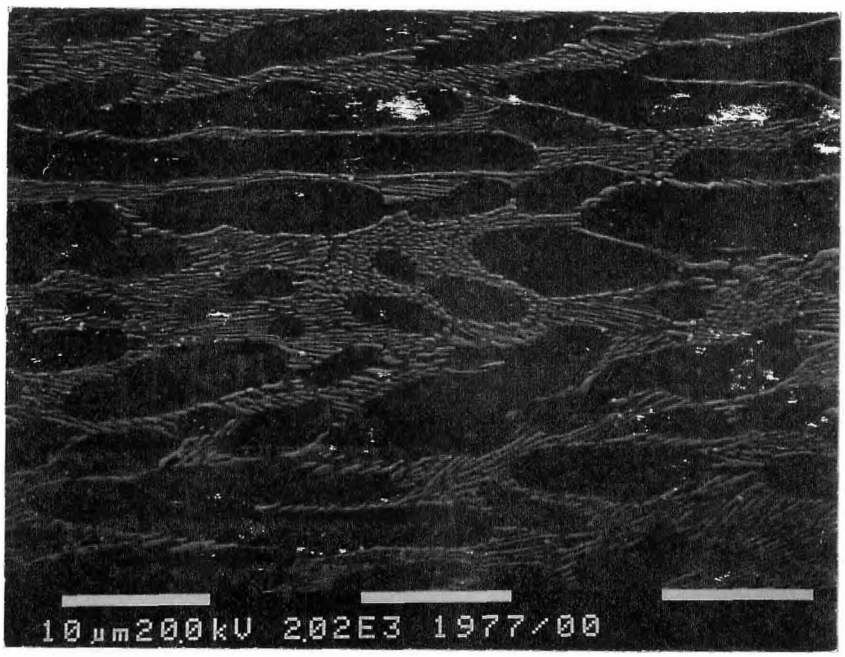

Figure 4-2 The Al-Fe Ohno cast rod at a higher magnification than Figure 4-1.

4.1.2 Al-Ni Ohno Cast Rod

The Al-Ni Ohno cast rod contained 5.1 wt% Ni and was cast at speeds of 524 mm/min and 769 mm/min. Figure 4-3 and 4-4 are SEM micrographs of the Al-Ni rod cast at 524 mm/min. The microstructure consists of primary aluminum dendrites and areas of Al-Al_3Ni eutectic which are evenly distributed throughout the cross section (as shown in Figure 4-3). Although the rod was directionally solidified, it is interesting to

note that the eutectic regions did not grow in a single direction and that some of these regions could be quite large in scale.(as shown in Figure 4-4).

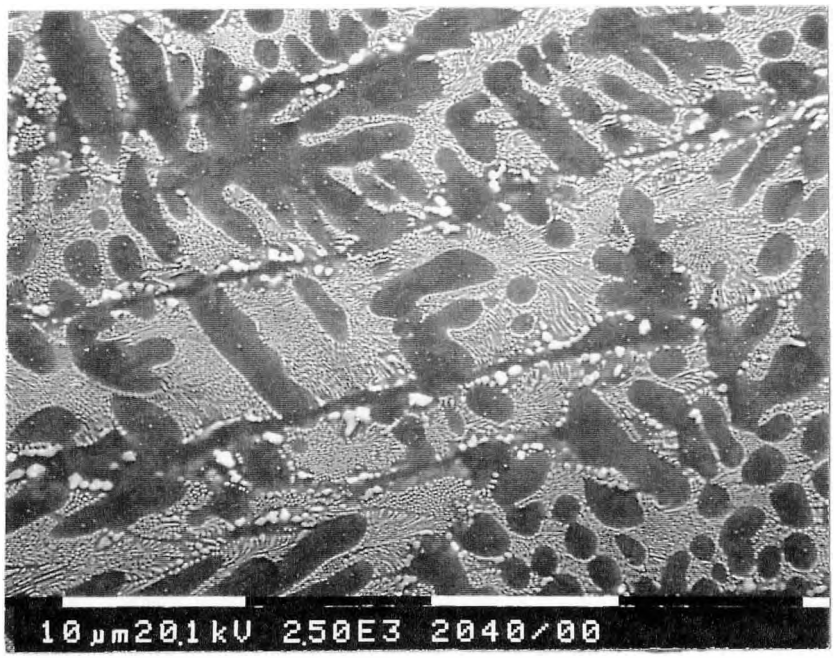

Figure 4-3 The Al-Ni alloy Ohno cast at 524 mm/min.

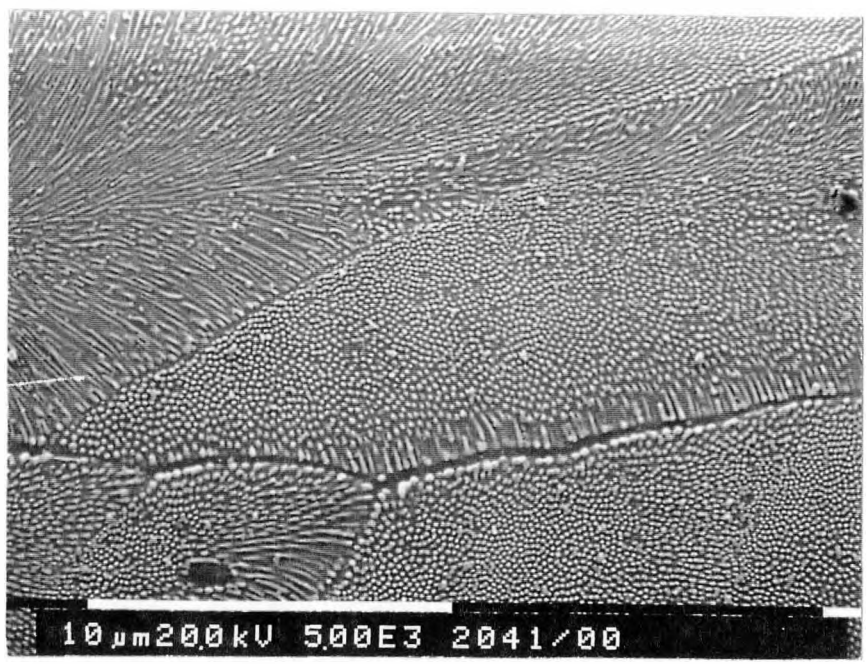

Figure 4-4 Regions of Al-Al_3Ni eutectic deviating from the growth direction.

The fibers in the rod cast at 524 mm/min were are approximately 75 to 100 nm in diameter and were separated by a spacing of 200 nm. The structure of the fibers in the alloys cast at 524 and 769 mm/min were determined to be Al_3Ni, both by x-ray diffraction and TEM diffraction. Casting at the higher speed (769 mm/min) proved to be more difficult to control. The resultant morphology of the alloy cast at 769 mm/min was that of a hypoeutectic Al-Al_3Ni alloy with fibers approximately 50 nm in diameter and spaced 125 nm apart. Figures 4-5 and 4-6 show cross sectional and longitudinal views respectively.

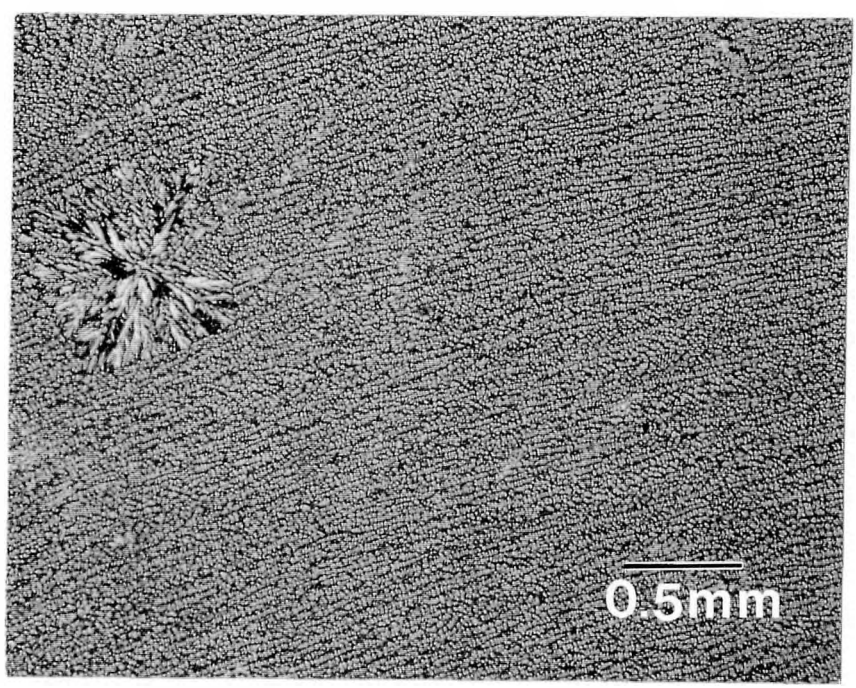

Figure 4-5 Cross sectional view of the Al-Ni alloy Ohno cast at 769 mm/min.

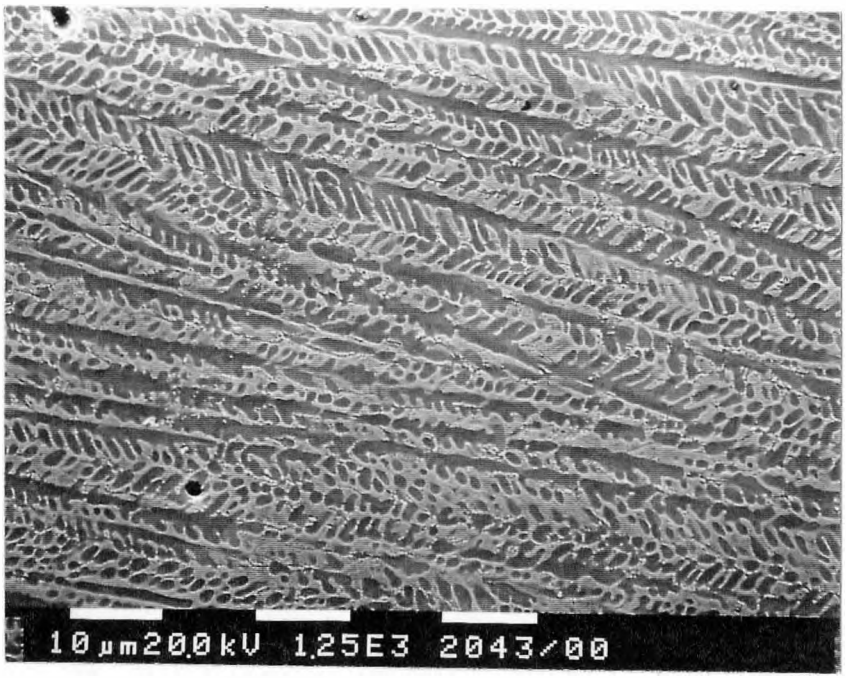

Figure 4-6 Longitudinal view of the Al-Ni Ohno cast at 769 mm/min.

It is also worthwhile to show how inclusions affected the morphology of the directionally solidified alloy. Figure 4-5 shows a dendrite that grew from an inclusion perpendicular to the casting direction. This phenomenon was common throughout the cross section of the structure.

4.1.3 Preparation of the Macrocomposite

The initial attempt to combine pure Al and pure Fe using the methods described in section 3.2 was not successful due to insufficient mechanical bonding. Figure 4-7 is a

schematic of the as cast macrocomposite, fabricated using the procedures described in section 3.2.

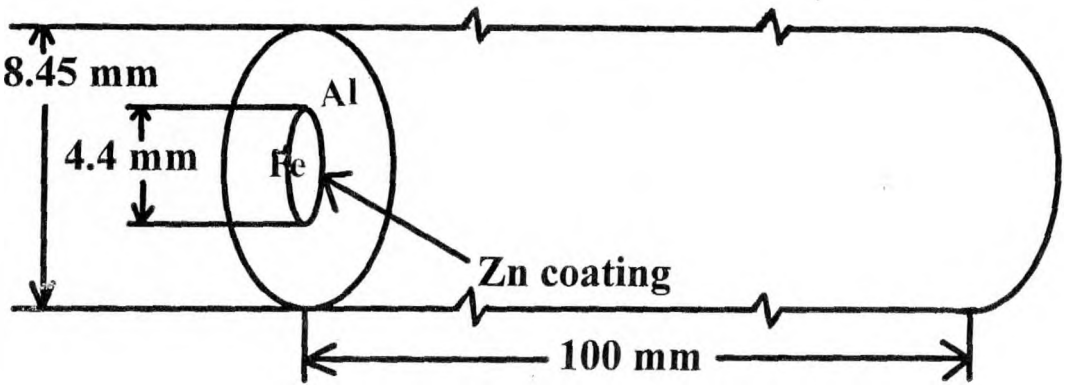

Figure 4-7 Schematic of the macrocomposite.

Figure 4-8 shows the layer of zinc between the Al and the Fe. The zinc layer was determined to be 0.3 mm thick. It provided a bond that was much more physically sound compared to the initial attempt at making a mechanical bond (as outlined in the experimental procedure section).

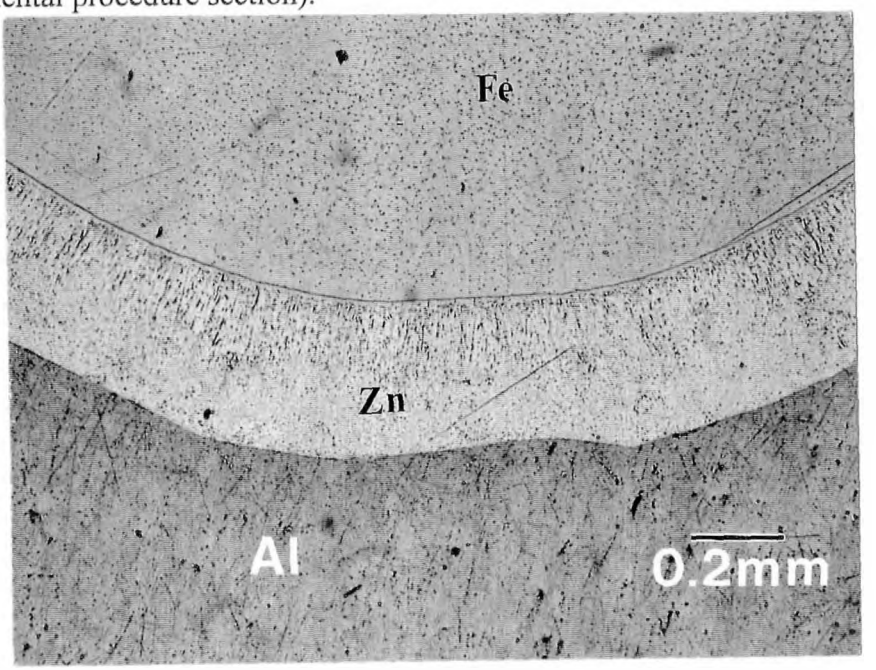

Figure 4-8 Cross section of Al-Fe macrocomposite.

4.2 Mechanical Properties

Each of the Al alloy rods was machined into billets as described in the experimental procedure and subjected to either tension or compression. The results of the tensile and compression tests are summarized in Table 4-1. True stress vs. true strain behavior was calculated from the tensile tests and can be seen in Figures 4-9a, 4-9b and 4-9c.

Material	Yield Strength (Tension-MPa)	Fracture Strength (Tension-MPa)	Apparent Buckling Stress (Compress-MPa)
Al-Ni OCC 524 mm/min	170	267	---
Al-Ni OCC 769 mm/min	230	307	---
Al-Fe OCC	121	327	218

Table 4-1 Summary of the tensile and compression tests.

For each of the tensile tests, the yield stress was taken at 0.2% offset. The true strain to fracture for the Al-Fe and Al-Ni alloy cast at 524 mm/min was ε=0.16, while the true strains to fracture for the Al-Ni alloy cast at 769 mm/min was ε=0.14. The fracture surface observations from the tensile tests will be discussed later in this section. Necking was only observed in the Al-Fe sample which experienced a 25% reduction in area at the fracture point.

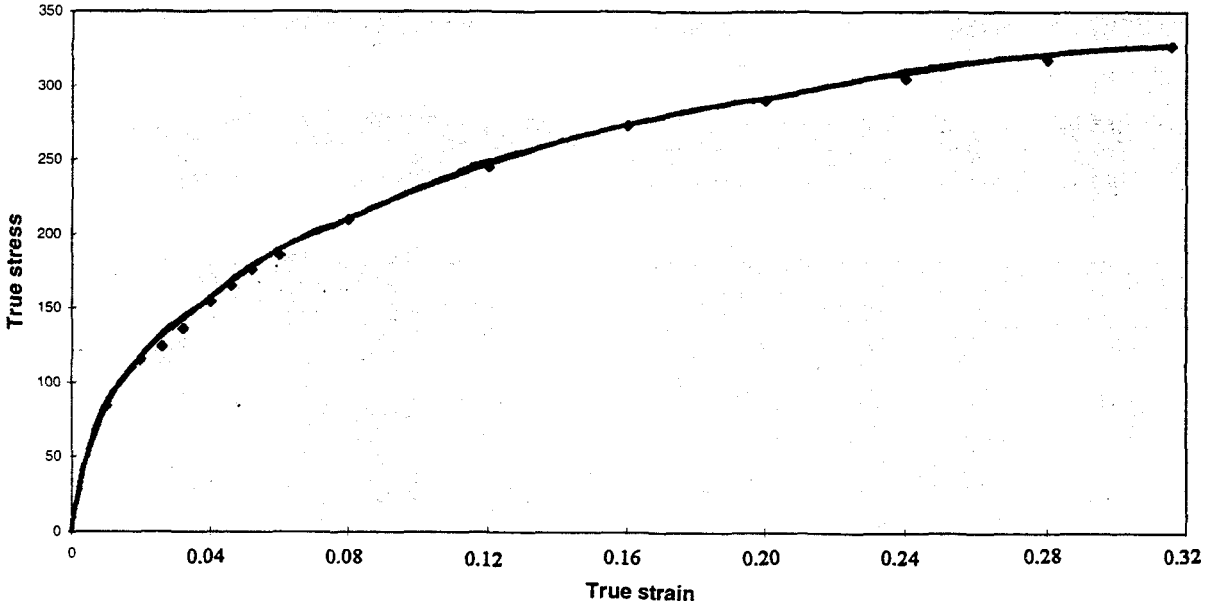

Figure 4-9a True stress vs True strain behavior for the Al-Fe Ohno cast alloy.

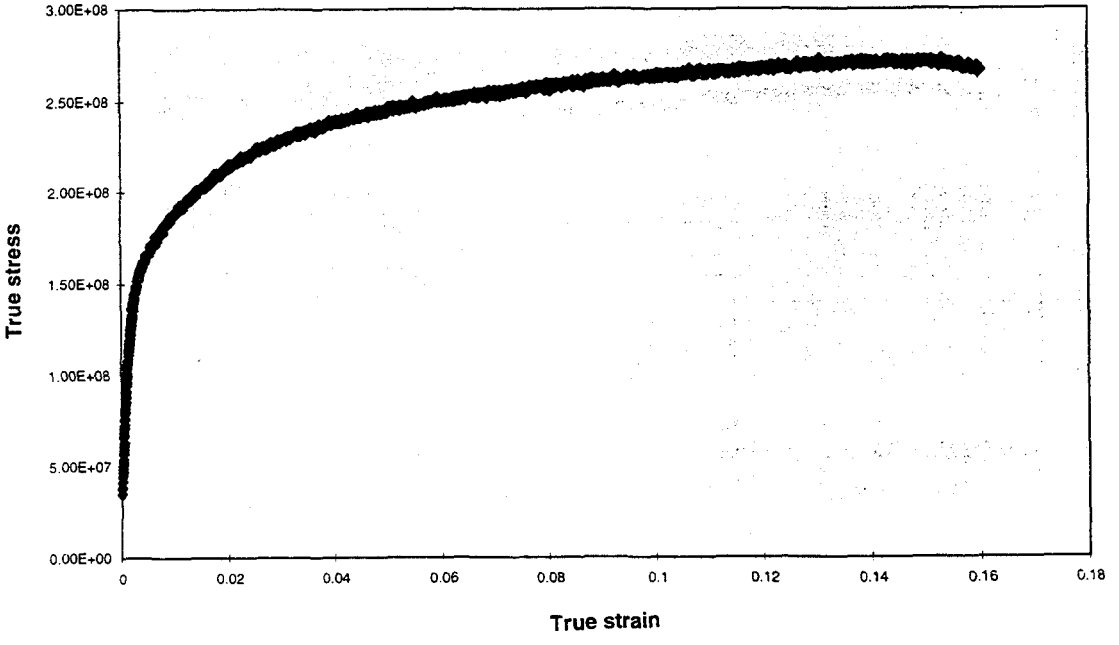

Figure 4-9b True stress vs. True strain behavior for the Al-Ni alloy Ohno cast at 524 mm/min.

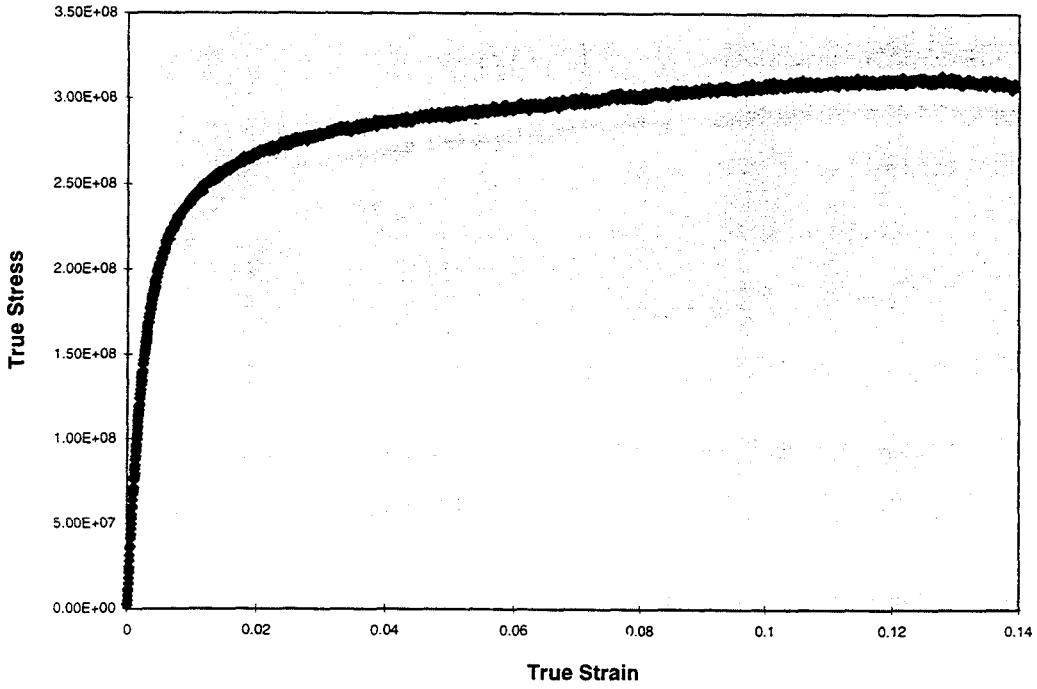

Figure 4-9c True stress vs. True strain behavior of the Al-Ni alloy Ohno cast at 769 mm/min.

The Al-Fe billet that underwent the compression test was found to have expanded by 33% in cross sectional area when the test was stopped. The compression specimen after testing was sectioned and observed to have a series of coarse shear bands making a 45° angle to the compression axis. After etching the section, the sample was observed in the SEM. The slip bands traveled through the material and caused the Al_6Fe intermetallic to undergo kinking as shown in Figure 4-10 (the compression axis in this figure is from the bottom to top of the page).

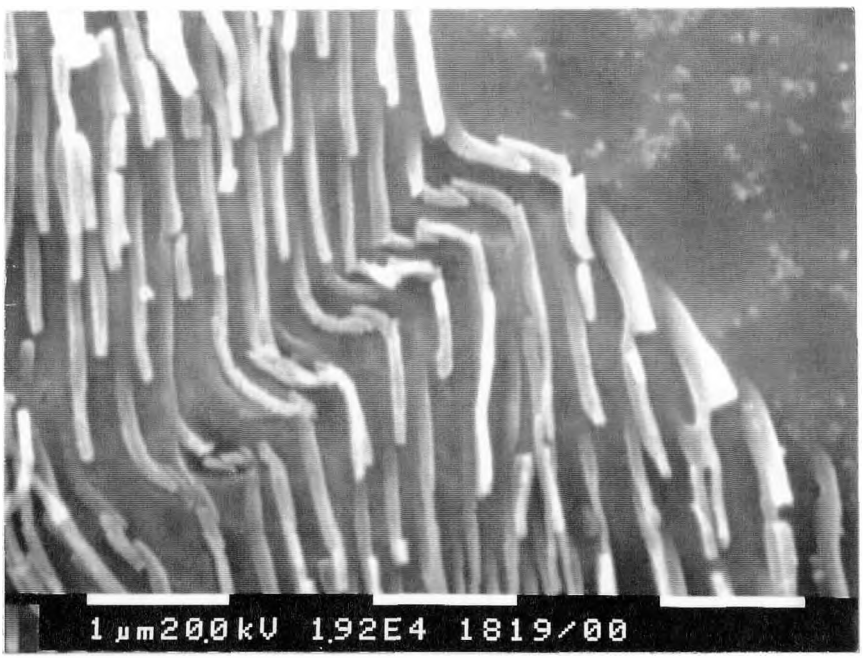

Figure 4-10 Kinking of the Al_6Fe intermetallic.

4.3 Hardness Tests

The hardness data is summarized in Table 4-2. There is a reasonable correlation between the yield strength obtained from the tensile tests and the hardness values from the as cast structures. The hardness values (DPH) have been converted to the equivalent yield strength in units of MPa by using the approximate relationship $H=3\sigma_y$. The yield strength of the Al-Fe rod was determined to be 121 MPa in tension and 159 MPa by hardness testing. The yield strength of the Al-Ni 524 cast* was measured to be 170 MPa in tension and estimated as 225 MPa from hardness tests. Finally, the yield strength of

the 769 cast** was measured to be 230 MPa in tension and estimated to be 247 MPa by hardness tests.

Material	Hardness (DPH)	Corresponding σ_y (MPa)
Al-Fe OCC as cast	48.59	159
Al-Ni OCC 524 as cast	68.79	225
Al-Ni OCC 769 as cast	75.51	247
Al-Fe OCC drawn to ε=1.4	69.49	228
Al-Fe OCC swaged to ε=2.0	60.19	197
Al-Fe hydrostatic extrusion to ε=0.5	67.30	220
Al-Ni OCC 524 swage to ε=1.4	92.72	303
Al-Ni 769 swage to ε=1.4	103.97	340

* Al-Ni 524 cast = Ohno cast alloy, solidified at 524 mm/min
**Al-Ni 769 cast = Ohno cast alloy, solidified at 769 mm/min

Table 4-2 Hardness Test Results.

The results shown in Table 4-2 also display how the hardness values vary after different processing steps. Limits imposed by the material or the equipment used to draw, swage or extrude the alloys dictated the strains used in these series of tests.

4.4 Large Strain Deformation

The large strain deformation imposed on the different alloys were produced by swaging, wire drawing or hydrostatic extrusion. This section will include details of the deformation of the Al-Fe and Al-Ni Ohno cast materials.

4.4.1 Al-Fe and Al-Ni Ohno Cast Materials

All the samples could be swaged successfully. After swaging, the microstructures of the Al-Fe and Al-Ni Ohno cast alloys were virtually the same, with fibers broken up in irregular fashion due to the strains imposed during swaging. Figure 4-11 is a micrograph of the Al-Fe rod swaged to a total strain of 2.0.

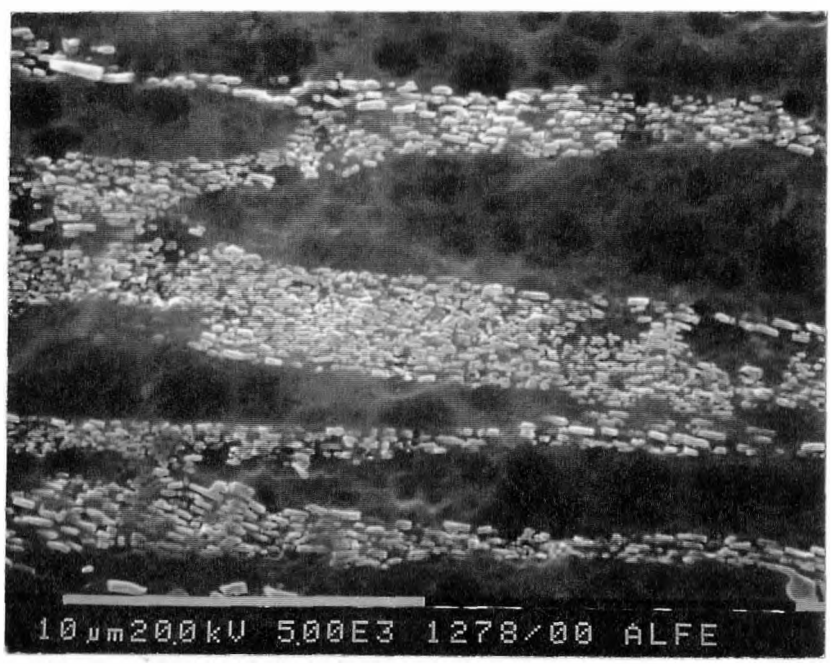

Figure 4-11 Swaged Ohno cast Al-Fe alloy.

The next step after swaging was wire drawing. The Al-Fe Ohno cast material was drawn successfully to a true strain of 1.4 after which the wire had accumulated enough damage to cause fracture. The failure occurred outside of the die and there was a

25 % reduction in area at the point of fracture. Figure 4-12 shows the microstructure after drawing to a strain of 1.4.

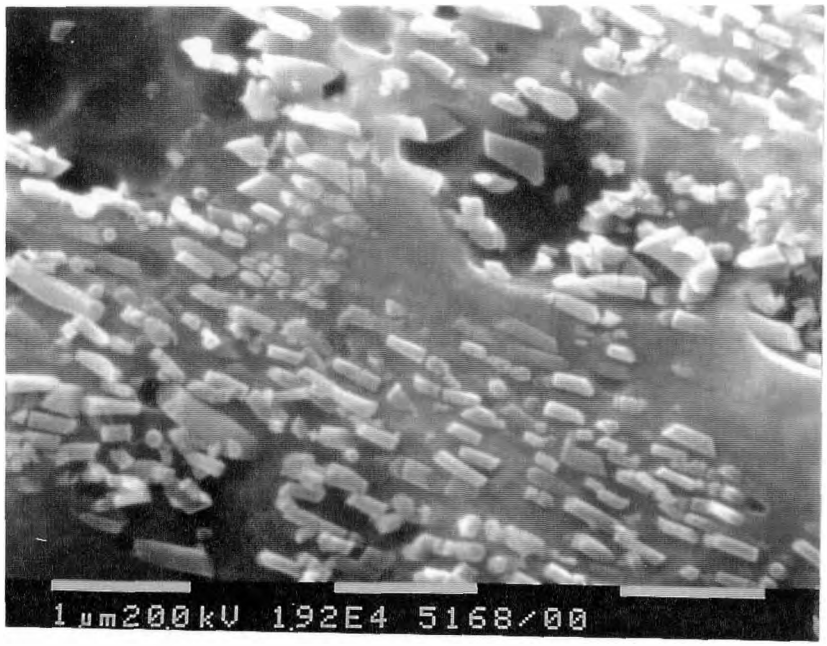

Figure 4-12 Ohno cast Al-Fe drawn to a strain of 1.4.

In Figure 4-12, there is no sign of significant plastic deformation of the fibers. The diameter of the fibers is essentially the same before and after drawing. In initial drawing attempts of the laboratory cast alloy (before Ohno casting of the material) large Al_3Fe particles that formed in the as cast alloy were observed breaking and voids opened up during drawing (Figure 4-13). The voids that opened up during drawing grew larger during each draw pass until eventually failure occurred. Upon analysis of the microstructure, there was evidence of V shaped voids opening up as a result of the voids formed by the cracked particles. The final fracture surface had a similar profile to the other smaller V shaped voids in the sectioned sample. It is apparent that the shear

stresses imposed in the die caused the small voids (due to cracking of the particles) to lead to fracture during drawing.

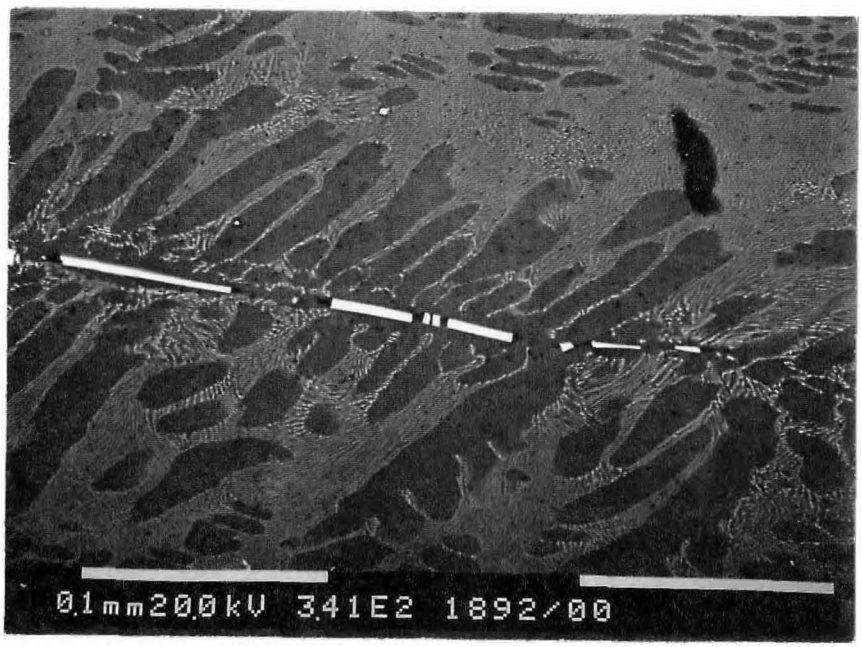

Figure 4-13 Coarse Al_3Fe particles fracturing during drawing.

The Al-Ni alloys were drawn only to a total strain of 0.2 and fractured at the die exit during drawing. There was insufficient deformation to permit an investigation into the strengthening of the Al-Ni due to wire drawing.

Hydrostatic extrusion was used in a series of tests to investigate whether the Al_6Fe phase could be plastically deformed at room temperature or not. A billet was extruded using a pressure of 500 MPa and chamber pressure of 375 MPa. Figure 4-14 is a plot of

extrusion pressure vs. displacement of the ram in the hydrostatic extrusion apparatus.. The total amount of strain imposed on the billet was 0.5. Figure 4-15 shows that the strain and hydrostatic pressure were sufficient to induce plastic deformation of the Al_6Fe particles. It is interesting to note the subtle physical differences in the extruded, drawn and swaged micrographs. In the swaged and drawn samples, there was no deformation of the fibers whereas in the hydrostatically extruded sample, the fibers did plastically deform.

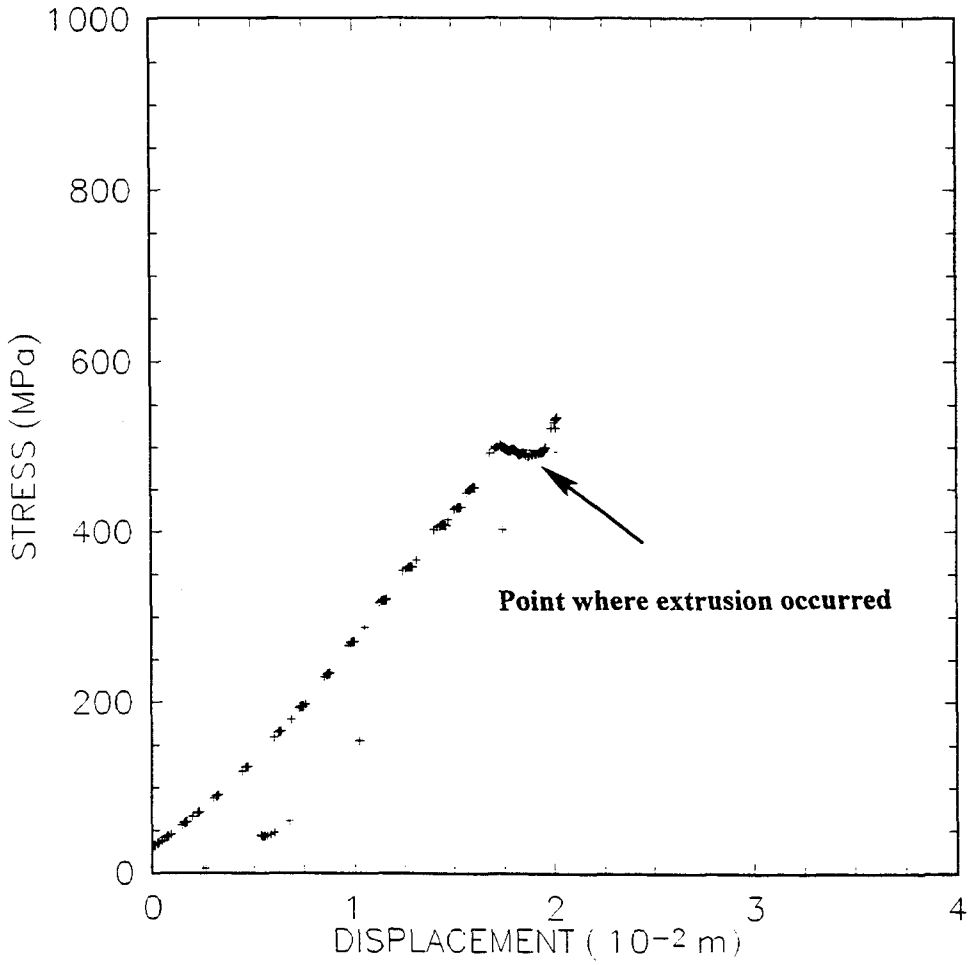

Figure 4-14 Plot showing extrusion pressure vs. displacement of the ram.

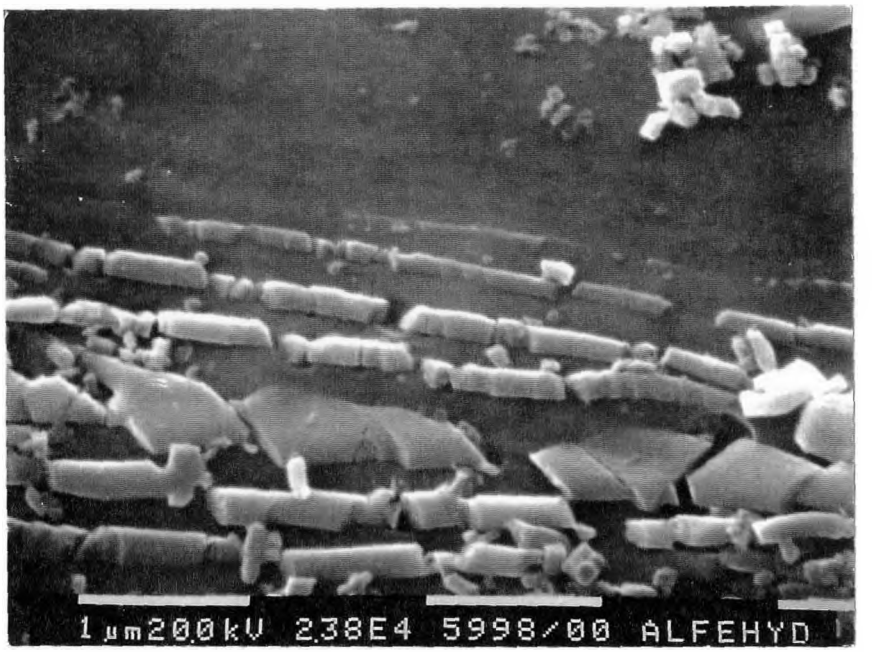

Figure 4-15 SEM micrograph of the Al-Fe OCC after hydrostatic extrusion.

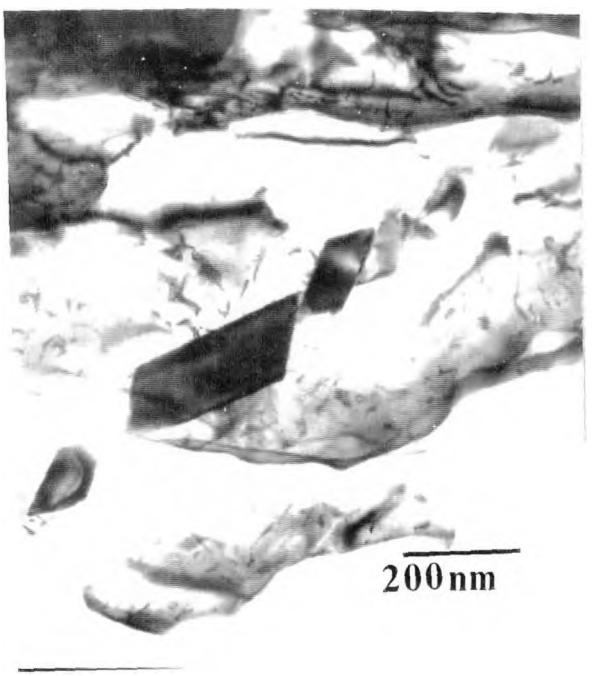

Figure 4-16 TEM micrograph of the Al-Fe OCC after hydrostatic extrusion.

A more detailed examination of the hydrostatically extruded sample was performed using the TEM. In Figure 4-16, the fibers have sheared and rotated slightly with respect to the growth axis of the fibers. Although the fibers did not undergo homogeneous plastic deformation, the fact that consistent deformation occurred in the fibers is a promising sign, i.e. with sufficient hydrostatic pressure, some deformation of the Al_6Fe is possible.

4.4.2 Deformation of the Al-Fe Macrocomposite

Initially, although the macrocomposite wire could be drawn, the Zn bond was insufficiently strong to allow any large strain deformation through wire drawing. After the macrocomposite was drawn to a strain of 0.4, the Fe and Al started to debond. Figure 4-17 is a micrograph showing delamination of the bond between the Al and Fe during wire drawing. Since the two materials were single phase and the main strengthening mechanism that could be used to harden the metals was cold working, the influence of swaging on mechanical properties was investigated. The results of the swaging tests are shown in Figure 4-18. By combining a material with a low work hardening rate (Al) with a material that has a higher work hardening rate (Fe), a composite with improved mechanical properties might be created by swaging. Although the sample was successfully swaged to a true strain of 2.57, metallography showed that the Zn layer did

not provide a sound mechanical bond between the Fe and the Al during swaging. Four different sectioned regions of the rod displayed an inconsistently thick Zn layer.

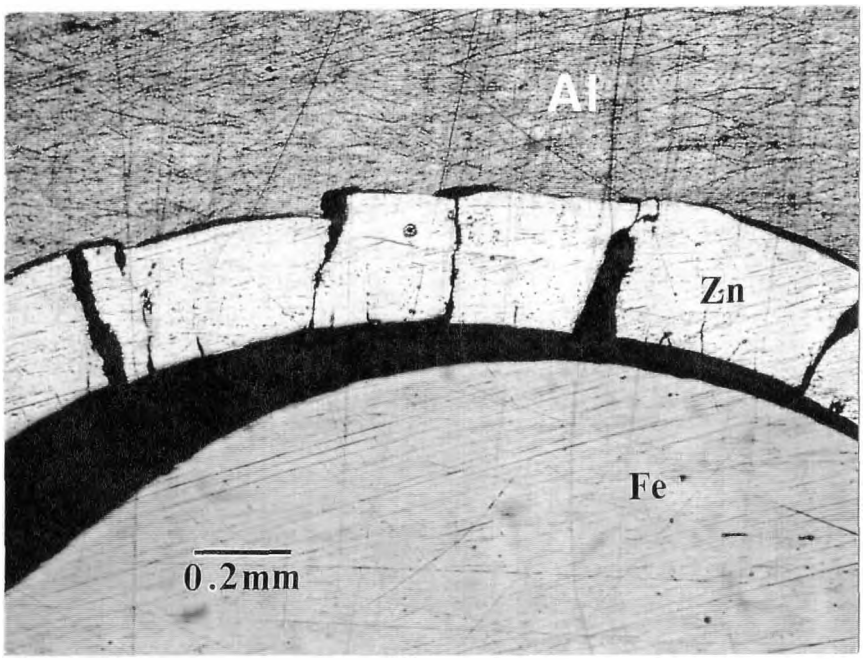

Figure 4-17 The Al-Zn-Fe bond after wire drawing.

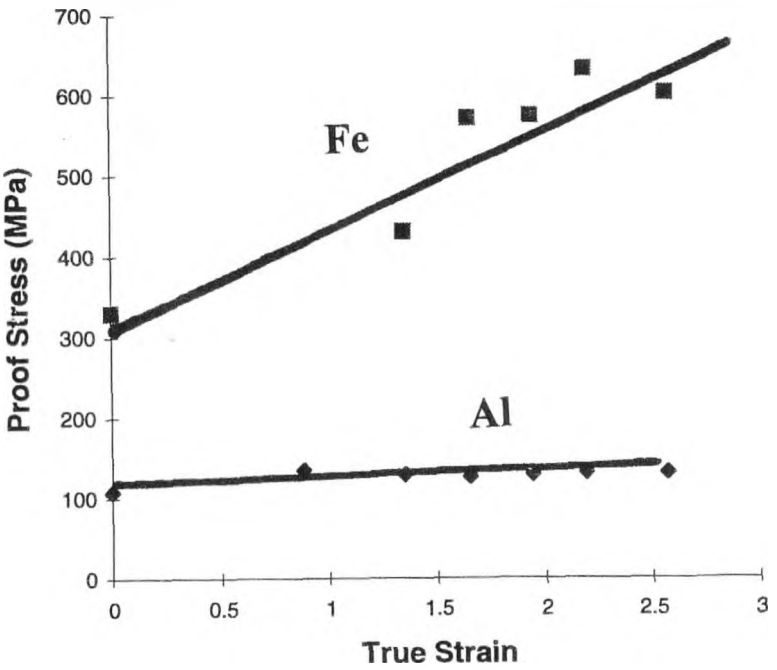

Figure 4-18 Effect of swaging on the hardness of the constituent materials.

4.5 Fractography

4.5.1 Al-Fe Ohno Cast Alloy

The fracture surface of the broken tensile sample shown in Figure 4-19a is characteristic of a purely ductile fracture. At higher magnification, distinct regions of ductile dimple fracture are apparent on the surface. The regions of pure Al in the as cast structure have diameters in the range of 1 to 6 μm. The fracture surface, i.e. the dimpled regions shown in Figure 4-19b have diameters in the range of 1 to 3 μm. Figure 4-19b represents only a small region of the total fracture surface, so it is likely that each of the dimpled regions corresponds to a region of pure Al. There is no clear indication as to the fracture process of the eutectic regions themselves. There are regions on the fracture surface that have Al_6Fe fibers on the outer region of the dimples and other areas where the fibers lie within the dimpled region. Thus, the dimples do not correspond to a region of Al in all cases, however, it is safe to state that the majority of the dimples correspond to a region of pure Al.

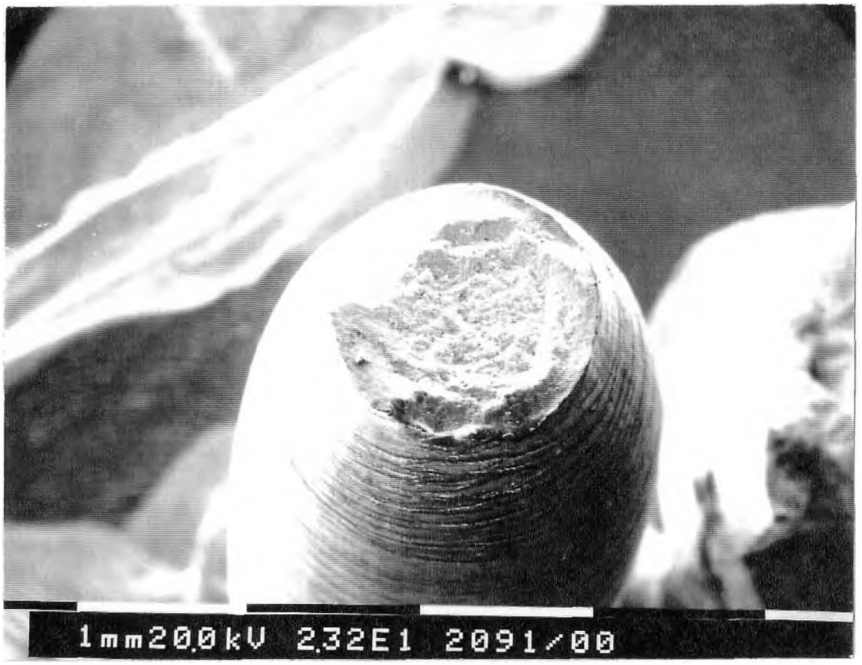

Figure 4-19a Fracture surface of the Al-Fe Ohno cast alloy.

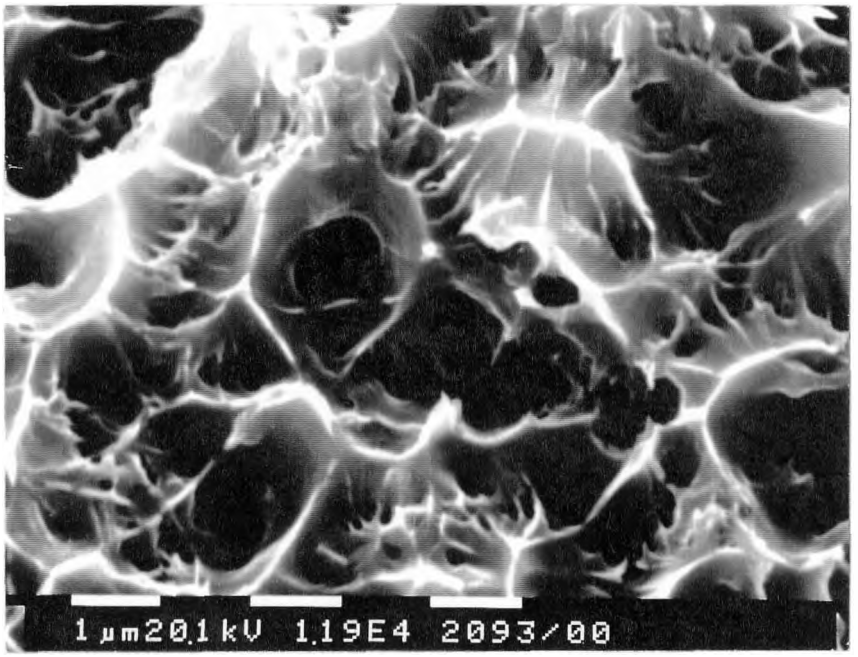

Figure 4-19b The Al-Fe Ohno cast alloy fracture surface at 12,000x magnification.

4.5.2 Al-Ni Alloy Ohno Cast at 769 mm/min

The fracture surface of the Al-Ni 769 cast is shown in Figures 4-20a and 4-20b. Figure 4-20a shows a fracture surface whose plane lies at 45° to the tensile axis. Closer examination of the fracture surface, as shown in Figure 4-20b, shows a surface that has undergone shearing and dimples that are elongated.

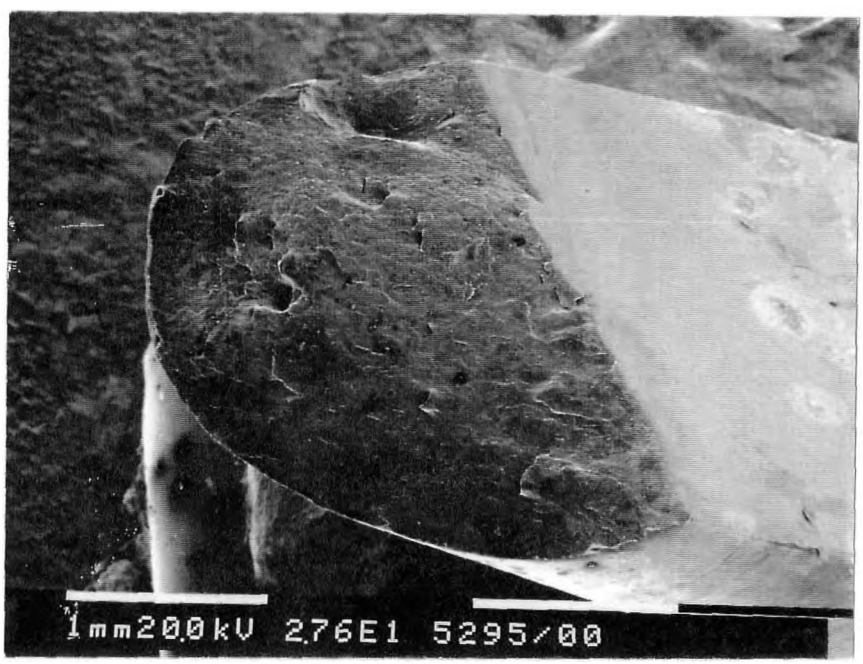

Figure 4-20a Fracture surface of the Al-Ni alloy cast at 769 mm/min.

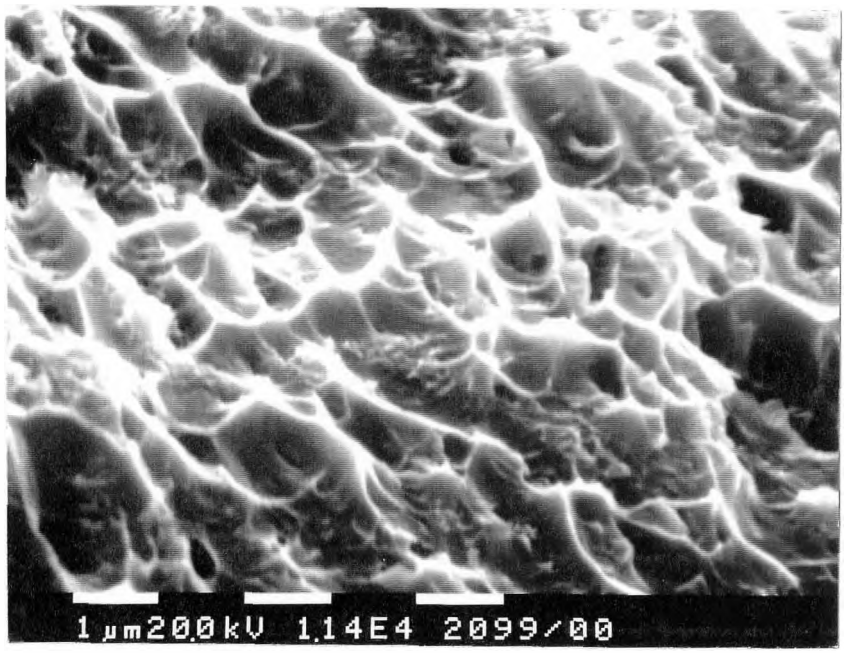

Figure 4-20b The Al-Ni Ohno cast alloy fracture surface at 11,400x magnification.

4.5.3 Al-Ni Alloy Ohno Cast at 524 mm/min

The Al-Ni cast fracture surface appears to be a combination of cooperative ductile and shear failure. Figure 4-21a shows the fracture surface from a polished longitudinal section. This micrograph is interesting because on the surface of the polished section, there are shear bands which are oriented 45° to the tensile axis. Figure 4-21b provides a closer look at one of the shear bands. The void that is seen to be opening up is contained in a region of the Al & Al_3Ni eutectic(this region is part of a rosette region found in the as cast alloy). Figure 4-21c shows how each of the bands have worked cooperatively to

produce an irregular fracture surface. A more detailed examination of Figure 4-21c helps one to determine the relationship between the fracture surface and the microstructure.

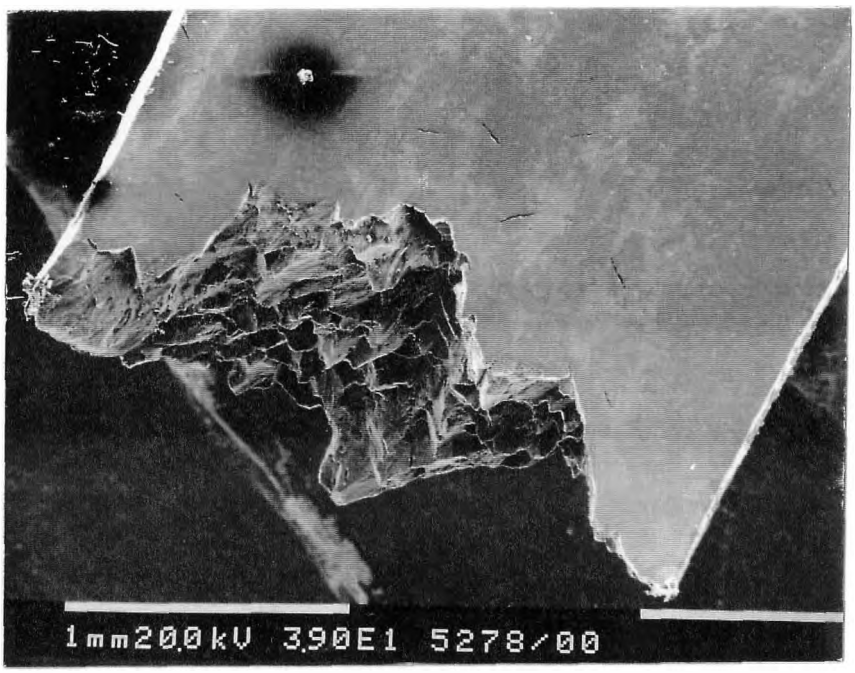

Figure 4-21a Fracture surface of the Al-Ni alloy Ohno cast at 524 mm/min.

Figure 4-21b Shear bands and void growth in the Al-Ni Ohno cast alloy.

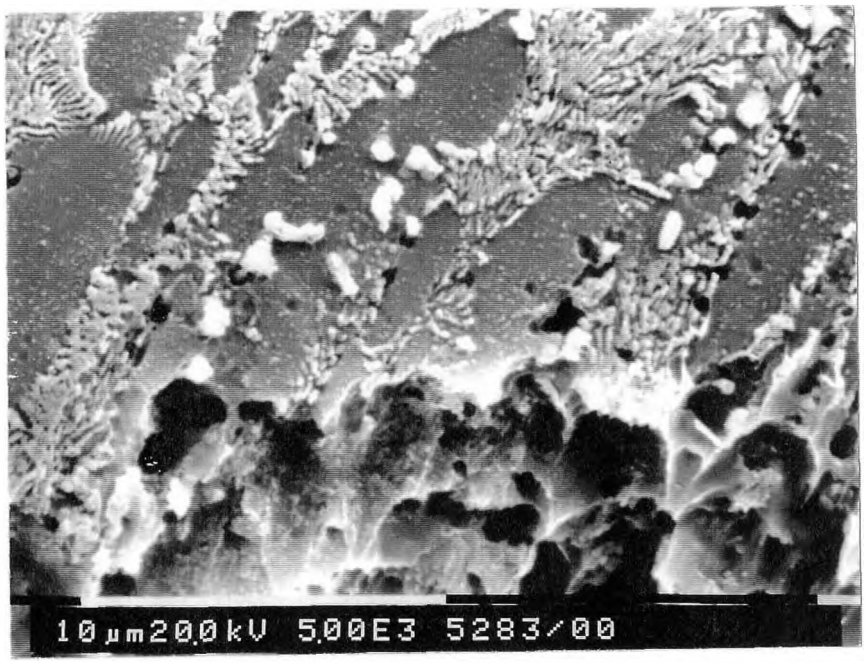

Figure 4-21c An examination of the fracture surface and longitudinal section.

4.4 TEM Analysis of the Al_6Fe Fibers

This section of the research was completed with the assistance of Muriel Veron of the Institute of Materials Research at McMaster University. This section outlines the work performed in an effort to explain the slip systems observed during deformation of the Al_6Fe phase.

The analysis began by determining the allowed reflections for Al_6Fe through determination of the structure factor. The atomic positions of each atom in the orthorhombic unit cell was keyed into a computer program ("Diffract") to assist in

determining the allowed reflections. The Al_6Fe unit cell has dimensions of a=6.49Å, b=7.44Å , c=8.79Å and contains 28 atoms. The allowed reflections as well as the interplanar spacing of each reflection is shown in Table 4-3. There are many allowed reflections in this complex system and one can appreciate how a measuring error might lead to ambiguities in the indexing process.

Plane (hkl)	d spacing (Å)		Plane (hkl)	d spacing (Å)
(001)	8.790		(122)	2.601
(010)	7.440		(113)	2.513
(100)	6.490		(030)	2.480
(011)	5.679		(212)	2.463
(101)	5.221		(220)	2.445
(110)	4.890		(031)	2.387
(002)	4.395		(221)	2.356
(111)	4.274		(130)	2.316
(012)	3.784		(023)	2.302
(020)	3.720		(131)	2.240
(102)	3.639		(004)	2.198
(021)	3.426		(203)	2.175
(112)	3.269		(123)	2.169
(200)	3.245		(300)	2.163
(120)	3.227		(032)	2.159
(201)	3.044		(222)	2.136
(121)	3.029		(014)	2.107
(210)	2.974		(301)	2.100
(003)	2.930		(213)	2.087
(022)	2.839		(230)	1.970
(211)	2.817		(302)	1.941
(013)	2.726		(231)	1.923
(103)	2.670		(033)	1.893
(202)	2.610		(024)	1.892

Table 4-3 Allowed reflections and interplanar spacings in the Al_6Fe system.

Analysis of the as cast and hydrostatically extruded samples in the Phillips CM12 TEM determined the growth direction to be in the direction of [001]Al_6Fe. The planes that sheared (as shown in Figure 4-16) were determined to be (012) by TEM diffraction. There are other areas in the alloy that shear has occurred but along the $(01\bar{2})$ plane.

High resolution TEM work on this Al_6Fe system has been initiated and is being continued by Muriel Veron. Initial observations have shown that the slip planes involved are (012) and $(01\bar{2})$. This work is continuing.

Hydrostatic extrusion proved to be a worthwhile experiment to refine this two phase material. In an experiment taking the Al-Fe Ohno cast alloy to a true strain of 0.5, deformation of the Al_6Fe (intermetallic) was observed. The ramifications of this experiment will be discussed in the following section.

5. Discussion

This chapter will explore the salient features of the results specific to microstructural evolution during Ohno casting, co-deformation and strengthening of materials presented in section 4.0. This section will also compare this work with the results from existing literature.

5.1 Characterization of the alloys

In a eutectic structure, traditional solidification theory states that the amount of undercooling determines the amount of free energy in the system and the lower the free energy, the higher the driving force for solidification to occur. The material will solidify at a critical undercooling (ΔT) either by homogeneous or heterogeneous nucleation. By increasing the solidification rate, one increases the amount of undercooling in the melt. This can best be described by the following equations from Porter and Easterling (1981) and which has been discussed by Elliot (1977);

$$v\lambda^2=\text{constant} \tag{5.1}$$

$$v/(\Delta T)^2=\text{constant} \tag{5.2}$$

where v is the growth rate(m/s), λ is the eutectic spacing and ΔT is the amount of undercooling. Equations 5.1 and 5.2 show that as the solidification rate, v is increased; (1) there is a decrease in the spacing of the eutectic and (2) the amount of undercooling in the melt is increased. The relevance of equation 5.1 to the current project is the fact that by increasing the solidification rate, one can decrease the spacing of the fibers which serves to produce a stronger material directly from the melt. Equation 5.2 is significant because as one increases the amount of undercooling in the melt, one deviates further and further from equilibrium. Therefore, the resultant microstructure is one which may contain non equilibrium phases. This was the case in the Al-Fe system studied in this project. The solidification speed of 85 mm/min was sufficient enough to produce a structure of metastable Al_6Fe eutectic plus primary aluminum. Despite much faster solidification speeds of 524 mm/min and 769 mm/min in the Al-Ni system, no metastable Al-Ni phases were present.

Both alloys were hypoeutectic and their microstructures agree with what has been experimentally determined by Hughes and Jones (1976) for the Al-Fe system and Barclay et al. (1971) for the Al-Ni system.

The Ohno caster was assumed to solidify these materials with a planar front. Both the Al-Fe and Al-Ni Ohno cast alloys had a cellular morphology. In cellular growth, each cell has virtually the same orientation as it's neighbors and together they form a single grain. For the Al-Fe system, observations of cellular growth was supported by a Laue pattern. The Laue pattern showed that there was a definite preferred orientation [001] along the growth direction. A study of an organic system by Hunt et al.(1966) found that if a binary eutectic alloy contains impurities, or if other alloying elements are present, the interface tends to break up to form a cellular morphology. The solidification direction

also may change as the cell walls are approached and the lamellar or rod structure fans out and may even change to an irregular structure, Figure 5-1.

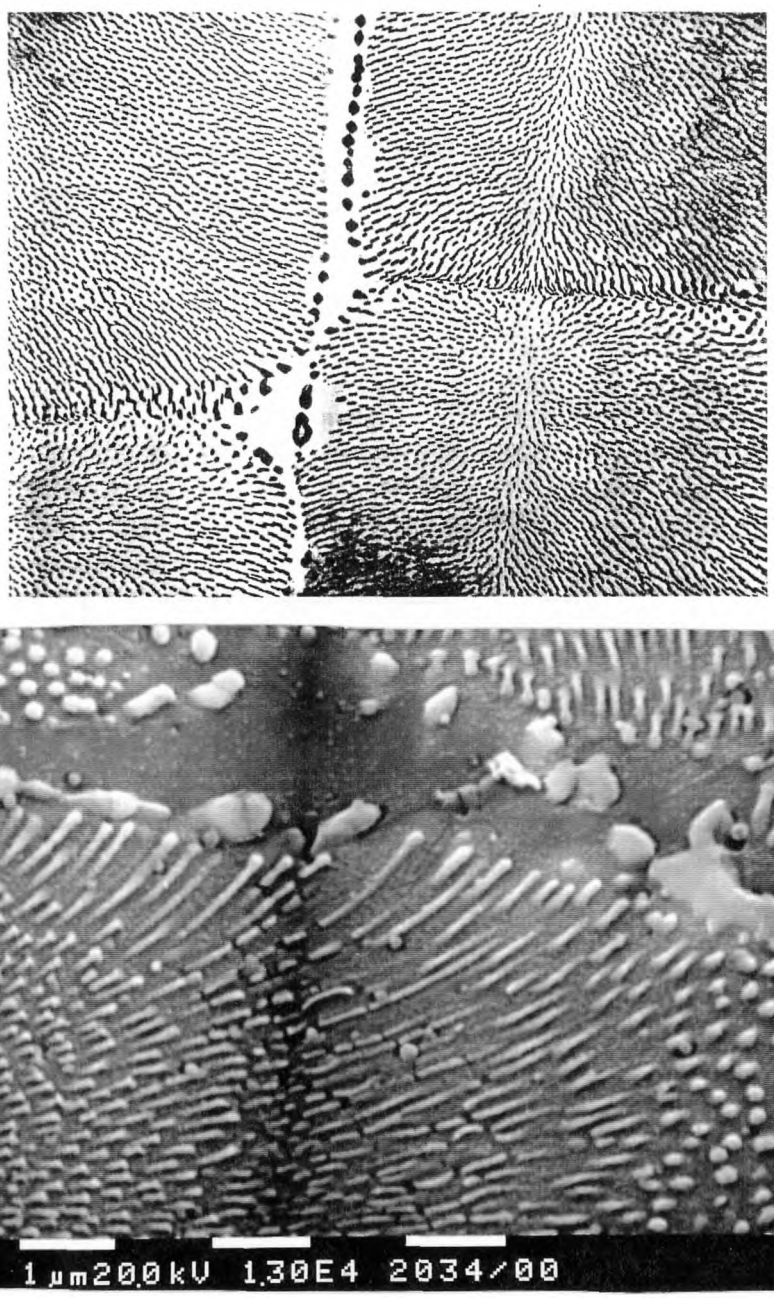

(a)

(b)

Figure 5-1 (a)Transverse section through the cellular structure of an Al-Al_6Fe rod eutectic (taken from Porter and Easterling (1981) and courtesy of J. Strid, University of Lulea, Sweden) and (b) The Al-Al_3Ni system studied in this project.

Figure 5.1 helps explain the appearance of the Al-Fe and the two Al-Ni Ohno cast alloys. In all three alloys, the eutectic fans out and/or becomes an irregular structure at the edges of the cellular network. The presence of impurities, at least in the Al-Ni system has been verified and evidence can be seen in Figure 4-5. These rosette type structures show that nucleation occurred ahead of the solid/liquid interface and these regions are present throughout the melt.

5.2 Mechanical Properties of the Alloys

The following section will review the properties of these alloys in tension and compression. The tensile and compression data will be used to determine and verify some of the mechanical properties of the fibers present in the Al-Ni and Al-Fe systems used in this study.

5.2.1 The Al_6Fe Fibers

The strength of the metastable Al_6Fe fiber is unknown. This section is dedicated to trying to determine the fracture strength of the fiber. The first thing to look at is the tensile data obtained from a simple tensile test. The Al-Fe Ohno cast sample fractured at a stress of 327 MPa. The volume fraction of fibers is V_f=0.05. Using the rule of mixtures approach can aid in determining the fracture strength of these fibers, the only unknown being the fracture strength of the matrix. It should be noted that the rule of mixtures approach to determining strength in a composite assumes that the fibers are continuous. The tensile strength of polycrystalline aluminum is on the order of 200 MPa (Ashby and

Jones(1980)). This alloy, however, contains fibers which restrict dislocation movement in the Al and can add strength by:

$$\tau = \mu b/l \tag{5.3}$$

which is known as the Orowan mechanism (Orowan (1948)). Although the fibers are not evenly distributed through the whole microstructure, the additive strength will be a rough estimate. In equation 5.3, τ is the additive strength, μ is the shear modulus, b is the Burger's vector and l is the interparticle spacing. Making the general approximation that μ=3/8(E) (where E is Young's Modulus) equation 5.3 becomes:

$$\tau = 3Eb/8l \tag{5.4}$$

Taking E = 70 GPa (from Ashby and Jones (1980)), b = 2.88 $x10^{-10}$ m and l = 500 $x10^{-9}$ m, equation 5.4 gives an approximate additive strength of 12 MPa. Since the additive strength due to the presence of the fibers is only 12 MPa, the overall strength of the matrix(Al) is 212 MPa. The contribution to strength due to the scale of the grain boundaries is considered to be negligible because the morphology is a cellular network and the size of the grains and their contribution to strength will already be considered in the 200 MPa figure. The rule of mixtures states:

$$\sigma_c = \sigma_m(1-V_f) + \sigma_f V_f \tag{5.5}$$

where σ_c is the strength of the composite, σ_m is the strength of the matrix, σ_f is the strength of the fiber and V_f is the volume fraction of fibers in the alloy. Substituting the

appropriate values into equation 5.5 gives a fiber fracture strength of 2.6 GPa. As stated earlier in the results section, the Al-Fe Ohno cast material was drawn successfully to a true strain of 1.4. The alloy was prepared for metallographic observation and it was determined the average aspect ratio (L/r) of the fibers was 6.8. Using equation 5.6 (Piggott (1980)), one can obtain a rough estimate of the fiber fracture strength.

$$\sigma_f/2\tau_i = L/r \qquad \textbf{(5.6)}$$

where L is the length of the fiber, r is the radius of the fiber and τ_i is the interfacial shear strength. For this situation; L/r = 6.8 and $2\tau_i$ = 200 MPa. Therefore, the fracture strength of the fiber is determined to be approximately 2.7 GPa. When using this method of analysis, measuring errors can occur which will affect the aspect ratio and so affect the value of the fracture strength. The comparison of these values to existing data will be discussed later in this section.

The Al-Fe Ohno cast alloy was also machined into billet form and subjected to a compression test between two platens. Metals are typically much stronger in compression than in tension which means that the magnitude of the stress to fracture a specimen in tension is much less than the stress required to fracture (buckle) a specimen in compression. For the Al-Fe sample, a 10 mm long specimen was compressed 70 % at a stress of 218 MPa. After metallographic observation, the material was recognized to have undergone buckling and the fibers were subjected to local shear. These shear bands are clearly evident across the whole sample, as shown in Figure 4-10. Figure 4-10 shows what is characterized as compressive kinking of a fiber composite. Fiber kinking has been the topic of a study by Budiansky et al. (1994) and Tao (1991). Since the fibers undergo kinking in compression, the material is much weaker in compression than in

tension. Thus, the amount one can compress this material is limited by buckling of the fibers.

The work of Kelly et al. (1986), Hull et al. (1985), Yue et al. (1968) and Tao (1991) have contributed to the derivation of the following expression based on Kelly's original model. When a shear instability is the dominant mechanism of failure:

$$\sigma = \tau_m/[\sin(\Theta \pm \Phi)\cos(\Theta \pm \Phi)] \qquad (5.7)$$

where σ is the yield strength of the composite, τ_m is the matrix shear yield strength, Θ is the fiber orientation with respect to the tensile axis and Φ is the degree of misalignment of the fibers. If the matrix shear yield strength, τ_m is 100 MPa, the fiber misorientation is $\pm 25^{\circ}$ and the value of Θ is zero, on substituting these values into equation 5.6 (taken from Tao (1991)), the yield strength of the composite is found to be σ = 260 MPa.

The experimentally determined value of the yield strength for the Al-Fe Ohno cast sample was 218 MPa. Thus, the experimentally determined value of the yield strength is in good agreement with the model presented by Kelly et al. (1986) and Tao (1991) which predicts a yield strength of 260 MPa.

5.2.2 The Al_3Ni Fibers

The two Al-Ni Ohno cast alloys were also machined into billets and pulled in tension. Equation 5.5 can also be used to determine the fracture strength of the Al_3Ni fibers. Again, there will be a correction for the strength of the matrix because of the presence of the second phase in the Al-Ni system. For the 524 cast alloy, E = 70 GPa, b = 2.88 10^{-10} m and l = 200 x10^{-9} m. The additive strength due to the presence of this

second phase is 16 MPa and so the overall strength of the matrix is approximately 216 MPa. Substituting the values of σ_c=230 MPa, V_f=0.12 and σ_m=216 MPa into equation 5.5 gives a fiber fracture strength of 0.6 GPa.

Using the same method of analysis for the 769 cast alloy, the corrected strength of the matrix is approximately 225 MPa. The appropriate values for the 769 Ohno cast alloy are σ_c=230 MPa, V_f=0.12 and σ_m=225 MPa. Substituting these values into equation 5.5 gives a fracture stress for the fibers of 0.7 GPa.

5.2.3 Discussion of 5.2.1 and 5.2.2

The fracture strength of the fibers in the 524 and 769 Al-Ni Ohno cast alloys are in good agreement with each other. The fracture strength of the fibers in the two alloys used in this study have been determined in the past to be on the order of 0.7 GPa. Hertzberg et al.(1965) studied the Al-Al_3Ni system and were able to extract fibers from the alloy. The fracture stress of these Al_3Ni fibers were found to range anywhere from 1.7 GPa to 2.8 GPa in their tests. In a study by Farag et al. (1975), the fracture strength of the Al_3Ni fibers was determined to be 2.1 GPa. Work done by Webb and Forgeng (1958) on the mechanical behavior of microcrystals has shown that the fracture strength of crystals such as Fe_3C and Mn_5Si_3 have ultimate tensile strengths that ranges from 2 GPa to 4 GPa.

The UTS of the Al_6Fe appears to be in good agreement with existing intermetallic data. The difference between the calculated value for the fracture strength and the experimentally determined values for the Al_3Ni fibers may be accounted for by a Weibull analysis (Weibull (1951)). The Al_3Ni fibers are inherently brittle and are obviously going to be weakened by the presence of flaws. If the largest fibers statistically contain the

largest number of flaws, the largest fibers will fracture first. In the Al-Al_3Ni system, the discrepancy between existing data for the fracture strength of Al_3Ni and the data obtained in this study and the heterogeneity of the cast structure might account for the observations. The inconsistency of the cast structure comes about because of the presence of 'rosette' regions (see Figure 4-21b). These 'rosette' regions most likely caused premature damage in the tensile test because these regions contained a series of fibers oriented perpendicular to the tensile direction. This discrepancy with literature data can be accounted for by the presence of flaws in the fibers and by accounting for the structure of the Al-Ni cast alloys. The calculated strength of the Al_6Fe fibers, however, shows good agreement with existing intermetallic data.

5.3 Fractography

The tensile tests for each of the three alloys produced three distinct fracture surfaces. In the case of the Al-Fe sample, the total strain to fracture was 0.16 and it failed in a ductile fashion. There was a reduction in area of approximately 25% at the point of fracture. In the Al-Ni 524 cast alloy, the total strain to fracture was 0.16 and the fracture surface was a cooperative ductile and shear failure. Finally, the Al-Ni 769 cast alloy underwent a total strain to fracture of 0.14 and the fracture surface was characteristic of a shear failure. In each of the samples, there was a sequence of damage events identified when the fracture surfaces were observed in the SEM. A relationship between the appearance of the voids on the surface and the scale of the solidified structure could be identified and micrographs are present in section 4.5. In a fiber reinforced composite, the ductility of the material is directly related to the volume fraction of fibers in the material. In the case of the Al-Fe Ohno cast alloy, the V_f of Al_6Fe fibers was 5%. The Al-Ni Ohno

cast alloy contained a V_f of Al_3Ni fibers equal to 12%. The tensile tests showed that the Al-Fe Ohno cast alloy failed in a ductile fashion and the Al-Ni Ohno cast alloy failed in a brittle fashion (by shear). The failure of the Al-Fe Ohno cast alloy was dominated by the nucleation of voids from fiber fracture. These voids were able to link up plastically and eventually cause a ductile failure. The failure of the Al-Ni Ohno cast alloys were dominated by the nucleation and growth of voids which linked up by shear. Therefore, by increasing the V_f of fibers in the alloys, one can create an increasingly brittle material(as was reflected in the tensile tests and wire drawing).

In tension there was no evidence of fiber deformation by plastic flow. The tensile test could be envisaged as a series of damage events that lead to fracture due to load transfer to the fibers.

5.4 Wire Drawing and Hydrostatic Extrusion

The first method used to try and induce co-deformation was wire drawing. In wire drawing of these two phase materials, there is a limit to the amount of strain that can be imposed because there is a competition between damage of the fibers and the ability to draw the material. In all alloys, it was found that the largest second phase particles were fracturing due to the difference in plasticity between the matrix and the second phase. As the drawing process proceeded, the voids grew and so the damage accumulated until the whole wire fractured.

The next step used to try and induce co-deformation was hydrostatic extrusion. Only the Al-Fe Ohno cast sample could be extruded because of the limited number of available extrusion dies. SEM and TEM analysis showed plastic deformation of the fibers was present. The mechanism of deformation was a simple shear process and the

slip planes were determined to be (012) and $(01\bar{2})$ for fibers having a [001] growth direction (Further analysis of this complex system is on-going in collaboration with Muriel Veron of the Institute of Materials Research at McMaster University).

The overview of these different processing experiments and results found to date brings us to the description of the limits that these materials have. The main problem encountered in this study was the lack of ease of deformation of the intermetallic. The intermetallic will only deform under hydrostatic pressure. Although both systems were two phase eutectic alloys, there is a big difference between these systems and the Cu-Nb system (Wood (1994)) and the Cu-Ag system (Frommeyer et al. (1975)). The Cu-Nb and Cu-Ag alloys can be drawn to ultra high strengths and ultra high strains because the materials have very similar yield strengths. The yield strengths of both Al and Al_6Fe and Al and Al_3Ni are at least an order of magnitude different. This translates into two materials that become very difficult to deform without inducing damage and eventually fracture.

An estimate of the correct stresses needed to plastically deform this material can be obtained by looking at a Mohr's circle construction for the most brittle phase in each of these systems. For the Al_6Fe system, we have established that the tensile stress must not exceed 2 GPa. What must be established is to find out what compressive stresses are needed in the die to adequately deform the brittle second phase. The fibers will deform plastically at or around their theoretical shear strength which is approximately $(\mu/50)/2$. Using the relationship $\mu = (3/8)E$ and taking $E = 200$ GPa, the theoretical strength of the fiber is estimated to be 1.5 GPa. The estimate of Young's modulus was taken from Westbrook et al. (1994) (This value was used because it is the value of E for two similar Al based intermetallic compounds, namely Al_3Ti and Al_3Zr). The theoretical strength of the Al_6Fe fiber is approximately 1.5 GPa. This is of the same order of magnitude as the

experimentally determined value. The approximate theoretical shear yield strength will be 750 MPa. Since this is the value we must obtain to plastically deform the fiber, we can establish what compressive stresses are needed from a Mohr's circle approach. If a stress of 500 MPa is applied along the tensile axis, a compressive stress of 1 GPa is required in order to induce deformation of the fibers. This estimate came from equation 5.8 (Beer et al. (1981)), which follows directly from Mohr's circle.

$$\tau max = 1/2 \mid \sigma max - \sigma min \mid \qquad \textbf{(5.8)}$$

Although the scale of the microstructure can be controlled by the speed of solidification, the intermetallic is difficult to deform. We have shown that a special stress state is required for deformation to occur, namely hydrostatic extrusion. This does not lend itself to being a mass production type of process. Therefore, an alternative route to a high strength product was studied, in the form of an aluminum macrocomposite. This contains Al and Fe that could be co-deformed to achieve high strengths.

5.5 The Al-Fe Macrocomposite

The initial investigation into the search for a new macrocomposite Al-Fe alloy proved to be promising. The work, although only in it's infancy, displayed the potential to develop into a material that could co-deform without fracture occurring. The only real draw back was that the interface between the Al and the Fe was not strong enough to allow for any extensive drawing. The Al-Fe macrocomposite was swaged, however, to a true strain of 2.57 and an overall yield strength of 395 MPa was obtained(via the rule of mixtures). The rod was not swaged further due to a limitation with the number of

swaging dies available. The trend was promising though, because the relationship between the increase in yield strength and the amount of strain imposed on the Fe appeared to be linear. The next logical step in this part of the study would be to look at the mechanical response of a pearlitic steel combined with an Al alloy. If an adequate bond can be achieved between the steel and the Al, the potential to produce a high strength two phase alloy would be much greater.

6. Conclusions

The essential features of this study of the development of an aluminum alloy for use as a high strength, high conductivity wire for use in electrical overhead transmission can be summarized as follows.

(1) There was limited success in the drawing of the Al-Fe and Al-Ni Ohno cast alloys. The main reason for this was because of the difference in yield strength between the two phases present in the alloys.

(2) Fracture occurred during drawing because of damage accumulation in the material caused by fracture of the fibers. The fibers in both alloys were observed to break first at the largest diameter fibers.

(3) Limited deformation of the intermetallic phase was observed using hydrostatic extrusion. Hydrostatic stresses of the order of 500 MPa were used to aid in inducing deformation of the brittle intermetallic phase present in the Al-Fe alloy. The slip planes were determined to be (012) and $(01\bar{2})$ with the fibers having a growth direction of [001].

Therefore, considering the investigation into future work of these alloys, two suggestions can be made. First, it will be worthwhile to investigate the deformability of these alloys with a much finer scale structure(nm) of intermetallic. Using the Ohno caster, one can produce fine diameter wires(< 4 mm) at speeds of 1 m/min. Casting an

alloy at 1 m/min would produce fibers of the order of 20 to 50 nm in diameter. Secondly, subjecting the material to hydrostatic stresses in an effort to induce co-deformation is also worthwhile because limited deformation of the intermetallic phase was observed in this study.

The final stage of this research was dedicated to the investigation of an Al-Fe "macrocomposite" as a possible two phase alloy to be used as an overhead conductor wire.

This macrocomposite was drawn to a limited value of strain because the bond between the Al and the Fe was insufficiently strong to allow extensive drawing. The macrocomposite, however, was swaged to a true strain of 2.57 and achieved an overall yield strength of 395 MPa. Therefore, if a stronger mechanical bond can be created between the Al and the Fe, drawability of the macrocomposite can be improved.

The best chance to obtain a high strength, high conductivity material for this application appears to lie in the development of a material like the macrocomposite, i.e. a two phase alloy where both phases have comparable yield strengths but different hardening rates ($d\sigma/d\varepsilon$). Producing an alloy with these characteristics will aid in the ability to draw to high strains. Therefore, meeting these conditions will be a prerequisite for high strength, high conductivity applications.

References

Ashby M. F. and Jones D. (1980) *Engineering Materials I*, Pergamon Press, Great Britain.

Barclay R. S., Kerr H. W. and Neissen P. (1971) *Journ. Mat. Sci.*, vol. 6, pp. 1168-1173.

Barczy P., Mertinger V., Gacsi Z. and Babcsan N. (1993) *Mat. Sci. Eng.*, vol. A173, pp. 137-141.

Berk J., Harbison J. P. and Bell J. L. (1979) *Journ Appl. Phys.*, vol. 49, p. 6031.

Brownrigg A., Spitzig W. A., Richmond O., Teirlinck and Embury J. D. (1983) Acta Met., vol. 31, p. 1141.

Budiansky B. and Fleck N. A. (1994) *Mechanics USA 1994, Appl. Mech. Rev.*, vol. 47, ed. A. S. Kobayashi.

Cahn R. W. (1989) *Met. Mater. Process.*, vol. 1, pp. 1-19.

Cantor B. And Cahn R. W. (1976) *Proceedings of the 2nd International Conference on Rapidly Quenched Metals*, Grant N. J. and Giessen B. C., eds., M.I.T. Press, p.59.

Dieter G. E. (1991) *Engineering Design: A Materials and Processing Approach*, 2nd edition, McGraw Hill.

Elliot R. (1977) *Eutectic Solidification, Review 219 in International Metals Review*, September, p. 161.

Embury J. D. and Fisher R. M. (1966) *Acta Met.*, vol. 14, pp. 147-159.

Farag M. M. and Flemings R. (1975) Met. Trans. A., vol. 6A, pp. 1009-1015.

Froes F. H. and Carbonara R. (1988) *J. O. M.*, February, pp. 20-27.

Frommeyer G. and Wasserman G. (1975) *Acta Met.*, vol. 23, pp. 1353-1360.

Gil Sevillano J., Van Houtte P., Aernouldt E. (1981) *Progress in Mat. Sci.*, Pergamon Press, Great Britain.

Hall E. O. (1951) *Proc. Roy. Soc.* (London), vol. B64, p. 26.

Hertzberg R. W., Lemkey F. D. and Ford J. A. (1965) *Trans. Met. Soc. AIME*, vol. 223, pp. 342-354.

Hollingsworth, E. H., Frank Jr., G. R. and Willet, R. E. (1962) *Trans. Met. Soc. AIME*, vol. 224, pp. 188-189.

Hughes I. R. and Jones H. (1976) *Journ. Mat. Sci.*, vol. 11, pp. 1781-1793.

Hull D. (1985) *An Introduction to Composite Materials*, Cambridge University Press, Cambridge, pp. 154-163.

Hunt J. D. and Jackson K. A. (1965) *Acta. Met.*, vol. 13, p. 1212.

Jones H. (1969) *Mat. Sci. Eng.*, vol. 5, pp. 1-18.

Jones H. (1994) *Mat. Sci. Eng.*, vol. A179, pp. 1-7.

Kelly A. and MacMillan N. H. (1986) Strong Solids, Claredon Press, Oxford.

Kurz W. and Gilgien P. (1994) *Mat. Sci. Eng.*, vol. A178, pp. 199-201.

Langford G. and Cohen M. (1975) *Met. Trans. A.*, vol. 6A, pp. 901-910.

Motoyasu G., Ohno A., Soda H. and McLean A. (1994) *33rd Annual Coference of Metallurgists; Recent Development in Light Metals*, August 20-25, Toronto.

Orowan E. (1948) *Discussion in the Symposium on Internal Stresses in Metals and Alloys*, Inst. Metals, London, p. 451.

Petch N. J. (1953) *J. Iron and Steel Institute*, vol. 174, p. 25.

Petty, E. R. (1961) *Journ. Inst. Met.*, vol. 89, pp. 343-349.

Piggott M. (1980) *Load Bearing Fibre Composites*, Pergamon Press, Toronto.

Porter D. A. and Easterling K. E. (1981) *Phase Transformations in Metals and Alloys*, Van Nostrand Reinhold Company, New York, pp. 222-230.

Rohatgi P. K. and Prabhakar K. V. (1975) *Met Trans. A.*, vol. 6A, pp. 1003-1008.

Salkind M., George F. and Tice W. (1969) *Trans. Met. Soc. AIME*, vol. 245, pp. 2239-2345.

Soda H., McLean A., Motoyasu G. and Ohno A. (1995*) Advanced Materials and Processes*, vol. 4/95, pp. 43-45.

Starke Jr. E. A. (1977) *Mat. Sci. Eng.*, vol. 29, pp. 99-115.

Tao S. (1991) *M. Eng. Thesis*, McMaster University, Hamilton, Canada.

Van Horne K. R. (1967) *Aluminum*, American Society for Metals, Metals Park, Ohio.

Verhoeven, J. D., Spitzig W. A., Schmidt F. A., Krotz P. D. and Gibson E. D. (1989) *Journ. Mat. Sci.*, vol. 24, pp.1015-1020.

Webb W. W. and Foregeng W. D. (1958) *Acta. Met.*, vol. 6, pp. 462-469.

Weibull W. (1951) *J. Appl. Mech.*, vol. 18, p. 293.

Westbrook J. H. and Fleischer R. L. (1994) *Intermetallic Compounds; Principles and Practice*, vol. 1, John Wiley and Sons, New York.

Wood J. T. (1994) *Ph. D. Thesis*, McMaster University, Hamilton, Canada.

Wood J. T., Embury J. D. and Ashby M. F. (1995) *Acta Materiala*, in press.

Zok F. (1989) *Ph. D. Thesis*, McMaster University, Hamilton, Canada.

Yue A. S., Crossman F. W., Vidoz A. E. and Jacobson M. I. (1968) *Trans. AIME*, vol. 242, p. 2441.

Zhou R., Smith J. L., Embury J. D. and Wood J. T. (1996) *"High Strength High Conductivity Cu-steel composites"*, Materials Characterization, in press.

Zok F. and Embury J. D. (1990) *J. Mater. Shaping Technol.*, vol. 8, pp. 77-81.